Monthly Notices of the ROYAL ASTRONOMICAL SOCIETY

MNRAS **512,** 2062–2081 (2022)
Advance Access publication 2022 March 7

https://doi.org/10.1093/mnras/stac592

Homogeneous transit timing analyses of 10 exoplanet systems

Ö. Baştürk,[1★] E. M. Esmer,[1★] S. Yalçınkaya,[1★] Ş. Torun,[1] L. Mancini,[2,3,4] F. Helweh,[5] E. Karamanlı,[5] J. Southworth,[6] S. Aliş,[7,8] A. Wünsche,[9] F. Tezcan,[10] Y. Aladağ,[11] N. Aksaker,[11,12] E. Tunç,[5] F. Davoudi,[13] S. Fişek,[7,8] M. Bretton,[9] D. F. Evans,[6] C. Yeşilyaprak,[10,14] M. Yılmaz,[1] C. T. Tezcan[10,14] and K. Yelkenci[7,8]

[1]*Ankara University, Faculty of Science, Astronomy & Space Sciences Department, Tandogan, TR-06100, Ankara, Turkey*
[2]*Department of Physics, University of Rome 'Tor Vergata', Via della Ricerca Scientifica 1, I-00133, Rome, Italy*
[3]*Max Planck Institute for Astronomy, Königstuhl 17, D-69117, Heidelberg, Germany*
[4]*INAF, Osservatorio Astrofisico di Torino, via Osservatorio 20, I-10025, Pino Torinese, Italy*
[5]*Bilkent University, Science Faculty, Physics Department, TR-06800 Ankara, Turkey*
[6]*Astrophysics Group, Keele University, Staffordshire ST5 5BG, UK*
[7]*Department of Astronomy and Space Sciences, Faculty of Science, Istanbul University, 34119 Istanbul, Turkey*
[8]*Istanbul University Observatory Research and Application Center, 34119 Istanbul, Turkey*
[9]*Baronnies Provençales Observatory, Hautes Alpes, Parc Naturel Regional des Baronnies Provençales, F-05150 Moydans, France*
[10]*Atatürk University, Science Faculty, Department of Astronomy and Space Sciences, 25240, Erzurum, Turkey*
[11]*Space Science and Solar Energy Research and Application Center (UZAYMER), University of Çukurova, 01330, Adana, Turkey*
[12]*Adana Organised Industrial Zones Vocational School of Technical Science, University of Çukurova, 01410, Adana, Turkey*
[13]*Department of Physics, University of Zanjan, P.O. Box 45195-313, Zanjan, Iran*
[14]*Atatürk University Astrophysics Research and Application Center (ATASAM), Yakutiye, 25240, Erzurum, Turkey*

Accepted 2022 February 25. Received 2022 February 25; in original form 2021 March 9

ABSTRACT

We study the transit timings of 10 exoplanets in order to investigate potential transit timing variations in them. We model their available ground-based light curves, some presented here and others taken from the literature, and homogeneously measure the mid-transit times. We statistically compare our results with published values and find that the measurement errors agree. However, in terms of recovering the possible frequencies, homogeneous sets can be found to be more useful, of which no statistically relevant example has been found for the planets in our study. We corrected the ephemeris information of all 10 planets we studied and provide these most precise light elements as references for future transit observations with space-borne and ground-based instruments. We found no evidence for secular or periodic changes in the orbital periods of the planets in our sample, including the ultra-short period WASP-103 b, whose orbit is expected to decay on an observable time-scale. Therefore, we derive the lower limits for the reduced tidal quality factors ($Q'_\star$) for the host stars based on best-fitting quadratic functions to their timing data. We also present a global model of all available data for WASP-74 b, which has a *Gaia* parallax-based distance value ∼25 per cent larger than the published value.

Key words: methods: observational – techniques: photometric – planetary systems – stars: individual: HAT-P-23, WASP-37, WASP-69, WASP-74, HAT-P-56, WASP-2, WASP-14, HAT-P-32, WASP-103, HAT-P-37.

1 INTRODUCTION

Analysis of exoplanet transit timing variations (TTVs) is important for several reasons. First of all, follow-up observations heavily rely on accurate and precise transit timings, especially those from space for which the observing window should be carefully planned. When ephemeris information is not up-to-date, at least a part of out-of-transit flux, or in worse cases, ingress/egress times may be missed due to the accumulation of uncertainties on their timings. Moreover, unseen additional bodies can be recovered from the periodic changes they cause in transit timings due to orbital perturbations and/or the so-called light time effect (Ballard et al. 2011; Ford et al. 2012; Agol & Fabrycky 2018). These multiplanet systems should be common, and it is also possible to determine the individual masses on the basis of the transit times of one or more transiting bodies in these systems without further and more challenging observations (Grimm et al. 2018). This enables a full characterization of the systems and their planets provided that they are also transiting (Agol et al. 2021). Most of the planets discovered by ground-based transit surveys are the so-called hot Jupiters because of their proximity to the host star. In these short-period orbits, they tidally interact with their host star causing them to lose angular momentum and even mass (Nortmann et al. 2018; Vissapragada et al. 2020). The long-term evolution of planets orbiting F- and G-type stars can be significantly

★ E-mail: obasturk@ankara.edu.tr (OB); esmer@ankara.edu.tr (EME); yalcinkayas@ankara.edu.tr (SY)

Table 1. Basic properties and the number of light curves analysed for each planet in our sample.

Planet name	P_{orb} (days)	M_p / $M_\star$ $\times 10^{-3}$	a/$R_\star$ –	$T_{eff,\star}$ (K)	Data base LC number	Literature LC number	Our LC number	Total
HAT-P-23 b[a]	1.212884(2)	1.77 ± 0.11	4.140 ± 0.230	5905 ± 80	41	39	5	85
WASP-37 b[b]	3.577469(11)	1.86 ± 0.30	9.017 ± 0.626	5800 ± 150	10	2	3	15
WASP-69 b[c]	3.8681382(17)	0.30 ± 0.02	11.968 ± 0.435	4715 ± 50	5	2	7	14
WASP-74 b[d]	2.137750(1)	0.64 ± 0.04	4.849 ± 0.038	5970 ± 110	3	35	4	42
HAT-P-56 b[e]	2.7908327(47)	1.61 ± 0.19	6.370 ± 0.110	6566 ± 50	18	0	2	20
WASP-2 b[f]	2.152226(4)	1.06 ± 0.22	8.463 ± 0.718	5200 ± 200	50	4	3	57
WASP-14 b[g]	2.243752(10)	5.79 ± 0.73	5.927 ± 0.370	6475 ± 100	24	13	2	39
HAT-P-32 b[h]	2.150008(1)	0.71 ± 0.01	6.050 ± 0.040	6207 ± 88	81	22	1	104
WASPP-103 b[i]	0.925542(19)	1.17 ± 0.08	2.978 ± 0.096	6110 ± 160	22	55	6	83
HAT-P-37 b[j]	2.797436(7)	1.20 ± 0.12	9.320 ± 0.570	5500 ± 100	85	4	2	91
Total					339	176	35	550

[a] Bakos et al. (2011). [b] Simpson et al. (2011). [c] Anderson et al. (2014). [d] Hellier et al. (2015). [e] Huang et al. (2015). [f] Collier Cameron et al. (2007). [g] Joshi et al. (2009). [h] Hartman et al. (2011). [i] Gillon et al. (2014). [j] Bakos et al. (2012).

different owing to the combined effect of magnetic braking and tidal dissipation. It has been argued by Damiani & Lanza (2015) that the existence of a quasi-stationary state, in the case of short-period planets, magnetic braking can significantly delay their tidal evolution that would, otherwise, bring the planet to fall into its host star. Angular momentum transfer between the orbital and rotational motion of the planet due to a potential spin-orbit coupling can induce observable deviations from a constant transit period (Lanza 2020). In systems with a transiting planet on a highly eccentric orbit, even apsidal motion can be observed (Patra et al. 2017; Bouma et al. 2019; Southworth et al. 2019; Bouma et al. 2020). In order to test such explanations of the observed orbital period modulations, the sample size of planets with in-depth analysis of their transit timings should be large enough to provide insight into the processes that lead to TTVs. Consequently, precise follow-up transit observations and their repeated analyses are needed to encompass the largest possible data sets of the systems, from which an observable TTV signal is possible for one reason or another.

We aim at a homogeneous analysis of the transit light curves of 10 exoplanets (HAT-P-23 b, WASP-37 b, WASP-69 b, WASP-74 b, HAT-P-56 b, WASP-2 b, WASP-14 b, HAT-P-32 b, WASP-103 b, and HAT-P-37 b) accumulated so far in the literature (176 in total for the planets in our sample) and various open data bases[1,2,3] (339 in total) as well as our own light curves (35 in total) from different observatories that are being published for the first time, adding up to 550 light curves in total (see Table 1 for details). The Transiting Exoplanet Survey Satellite (TESS) has observed only two of our targets (HAT-P-32 and HAT-P-37), one of which (HAT-P-32) has only long-cadence data, and the other (HAT-P-37) was blended by a bright source not resolved by TESS, making both inadequate for precise measurements of the mid-transit times. We are therefore limited to ground-based observations. We also note that HAT-P-56 b is being observed by TESS at the time of our study during sectors 43, 44, and 45.

We describe the instruments that we used for transit observations of the planets in our sample, the data reduction techniques that we employed, and the quantitative criteria for light-curve selection procedure in Section 2. Information on light-curve modelling, mid-transit time measurements, the TTVs, and the updated ephemeris based on the underlying data sets is presented in Section 3. We then analyse the mid-transit timings, search for potential secular and/or periodic changes in the orbital periods of the planets we study, and compare the data sets composed of homogeneous measurements that are based on our own measurements of mid-transit times with those that consist of the measurements by the observers from the same light curves. We also refine the parameters of the transiting exoplanet WASP-74 b based on the global model of the target's most precise light curves acquired so far, radial velocity (RV) measurements including our own measurements from unpublished HARPS archival data, broad-band magnitudes that we gathered from different data bases, reliable stellar atmospheric parameters from the literature, and the ultra-precise distance value based on its *Gaia* parallax, which is ∼25 per cent higher than the value referred to in the literature (Section 3.3.5). Finally, we discuss our results in Section 4.

2 OBSERVATIONS AND DATA REDUCTION

2.1 Observations

2.1.1 TUG T100 observations

We observed 14 transits in total with the 1-m Turkish telescope T100, located in TÜBİTAK National Observatory of Turkey's (TUG) Bakırlıtepe Campus at 2500-m altitude. With the well-established defocusing technique (Southworth et al. 2009; Baştürk et al. 2015), we achieved high precision in photometry of our stars using a cryo-cooler SI 1100 CCD with 4096 × 4096 pixels, which gives an effective field of view (FoV) of $20' \times 20'$. We employed a Bessell *R* filter in our exposures, the times of which were determined according to the brightness of the target, the duration of the observed transit, and the apparent proximity of nearby stars on the CCD to obtain the best signal-to-noise ratio (SNR).

2.1.2 CAHA observations

We observed three transits of WASP-69 b, two transits of WASP-103 b, and one transit of HAT-P-23 b using the 1.23-m telescope at the Calar Alto Observatory (CAHA), Spain, equipped with the DLR-MKIII CCD camera. Two transit light curves of WASP-69 b were obtained through a Cousins I_c filter, while one light curve for the same target was acquired in the Sloan i' passband on 2016 September 8. One WASP-103 b light curve was obtained in the Cousins R_c filter and another in the Sloan-r' filter. The FoV was $21'.5 \times 21'.5$ at a

[1] http://var2.astro.cz/ETD/index.php
[2] https://www.exoclock.space/
[3] http://brucegary.net/AXA/x.htm

plate scale of 0″.32 per pixel. We used the defocusing technique in the observations to increase photometric precision.

2.1.3 IST60 observations

We observed a transit of WASP-74 b on 2020 August 14 with the 60-cm telescope (IST60) of Istanbul University Observatory (IUGUAM), located at the Çanakkale Onsekiz Mart University Ulupınar Observatory, Turkey, at 410-m altitude above sea level. IST60 is a Ritchey-Chrétien (RC) telescope on an NTM-500, German equatorial mount. An Andor iXon Ultra 888 model CCD is attached at its focal plane. This setup gives a pixel scale of 0″.56 per pixel and a FoV of 9.6 × 9.6 arcmin^2.

2.1.4 UT50 observations

The transits of WASP-37 b on 2020 May 5 and HAT-P-23 b on 2021 July 20 were observed with the 50-cm RC telescope, equipped with an Apogee Aspen CG-type CCD at Çukurova University UZAYMER Observatory's campus in Adana, Turkey. The CCD has 1024 × 1024 pixels with a pixel scale of 2″.4 per pixel, which gives a similar effective FoV of T100. The details of the observatory and observing conditions are provided in Poro et al. (2020). We made use of the standard Johnson *R* filter during the observation of HAT-P-56 b transiting its star, while the observation of WASP-37 was acquired without a filter (clear) to increase the SNR.

2.1.5 ATA50 observations

We observed a transit of WASP-14 b on 2020 May 14 and a transit of WASP-2 b on 2020 October 12 using the 50-cm aperture, RC telescope, located at Atatürk University's ATASAM Observatory in Erzurum, Turkey, at an altitude of 1824 m above sea level. An Apogee Alta U230 CCD with 2048 × 2048 pixels of 15-μm size was employed, giving a pixel scale of 0″.77 per pixel. Unfortunately, we had a dome failure at the end of this observation, and we were not able to use it again throughout our study. We made use of a Cousins R_c filter in the observation and defocused the target slightly to be able to expose for a longer duration and thus increase the SNR.

2.1.6 T35 observations

We used the 35-cm T35 telescope in Ankara University Kreiken Observatory (AUKR) primarily to check the reliability of the ephemeris information for the transit observations of our targets. When the weather conditions are optimal, it is also possible to achieve the required precision in photometry to derive mid-transit times having uncertainties smaller than ∼2 min. We observed 10 transits in total with this telescope and the 1024 × 1024 Apogee Alta U47 CCD attached at its focal plane. Only the transit light curve of WASP-103 b on 2018 July 1 was obtained without a filter, while the rest of the light curves were acquired through the Bessel *R* filter.

We summarize the basic information about the telescopes that we employed for data acquisition in Table 2.

Table 2. Basic information on the instruments that we employed in our observations.

Telescope Label	Aperture cm	Camera px × px	FoV arcmin^2	Plate scale ″ / px
T100	100	4096 × 4096	20.0 × 20.0	0.11
CAHA	123	2048 × 2048	21.5 × 21.5	0.32
IST60	60	1024 × 1024	9.6 × 9.6	0.56
UT50	50	1024 × 1024	11.2 × 11.2	2.40
ATA50	50	2048 × 2048	12.4 × 12.4	0.77
T35	35	1024 × 1024	13.2 × 13.2	0.75

2.2 Data reduction

We corrected our images acquired with T100, IST60, UT50, ATA50, and T35 with the AstroImageJ (hereafter AIJ) software package (Collins et al. 2017) for the instrumental effects (bias-dark-flat corrections) in the standard manner by making use of calibration images obtained in the same nights with the observations. We employed 2 × 2 pixel binning when needed to decrease the exposure and readout times. We converted all the observation timings to Dynamical Barycentric Julian Days (BJD-TDB) before an ensemble photometry (Honeycutt 1992) with the AIJ relative to a number of comparison stars, selected according to their brightness, colour, and the unchanging behaviour during an observing run in the passband of observations. We determined the centres of the apertures visually to avoid incorrect flux-centre positions by centroid methods when applied to 'ring-like' shapes of the stellar signal on CCD images due to defocusing. We then corrected for the airmass and then normalized the relative fluxes determined by the AIJ with the line fit to the out-of-transit relative fluxes.

CAHA raw images were reduced by using the DEFOT code (Southworth et al. 2014 and references therein), which performs aperture photometry using the APER algorithm. Differential photometry was performed with respect to an ensemble of comparison stars, the number of which depends on the availability of adequate stars with constant flux within the limits of the observation setup during an observing night.

Finally, we detrended the light curves from red noise by making use of Gaussian processes since instrumental effects such as the drifts in the x–y positions of targets and comparison stars on the CCD images, and non-linearity issues as well as astrophysical noise sources such as stellar variability and spot-induced asymmetries affect transit profiles differently for each of the stars in our sample. We used a quasi-periodic kernel for the stochastic part of a light-curve model, the deterministic part of which was composed of a dilution factor, mean out-of-transit flux, and the transit model based on the system parameters from the studies announcing their discoveries. These parameters were also used during the light-curve modelling to derive the mid-transit timings for consistency since they are the default values provided by the NASA Exoplanet Archive for a given planet. We checked the level of scatter in the light curve in the out-of-transit flux through the standard deviation and tried to preserve it to avoid decreasing the level of white noise artificially in the data during the process.

We present a log of all our observations in Table 3 to provide statistical information summarizing the quality of our observations. We also provide all the acquired light curves in the Appendix A and the data in the online materials as well as their noise statistics separately in relevant files for each of the planets together with that from the light curves of others.

2.3 Light-curve selection criteria

Quality light curves are needed to infer mid-transit timings, precise enough to study potential transit timings in a system. On the other hand, the number and the frequency of observations are also crucial to

Table 3. A log of photometric observations performed for this study. The dates of the light curves that are eliminated and hence not used in the TTV diagrams are marked and the reasons for the elimination are given in the footnotes.

System name	Telescope	Date UTC	Start UTC	End UTC	Filter	Exp. time (s)	Images number	PNR	β	Mid-transit BJD–TDB	Error (days)
HAT-P-23	T100	2014-09-25	17:32:33	20:24:20	R	135	65	0.357	0.529	2456926.300832	0.000181
HAT-P-23	CAHA	2015-08-28	19:43:29	01:54:53	R_c	40	511	2.288	0.344	2457263.483520	0.000259
HAT-P-23	T35	2019-08-08	20:05:30	01:00:02	R	60	285	10.263	0.546	2458704.391921	0.001378
HAT-P-23	T35	2019-09-28[a]	17:38:08	22:45:35	R	90	188	5.911	0.401	2458755.329150	0.001652
HAT-P-23	UT50	2021-07-20[b]	19:06:30	22:39:37	R	150	78	1.340	1.542	2459416.355578	0.001028
WASP-37	T100	2017-04-27	20:45:50	01:28:57	R	135	105	0.974	0.624	2457871.472553	0.000692
WASP-37	UT50	2020-05-28[a, b]	18:19:19	22:56:44	Clear	60	236	10.118	2.018	2458998.368941	0.000917
WASP-37	T100	2020-06-22[c]	20:55:51	23:59:47	Clear	125	70	1.933	0.853	2459023.423285	0.001028
WASP-69	CAHA	2015-08-22	19:47:03	01:05:04	I_c	50	316	0.971	0.238	2457257.407761	0.000155
WASP-69	CAHA	2015-09-18	19:44:12	01:04:23	I_c	75	254	0.962	0.454	2457284.484812	0.000162
WASP-69	CAHA	2016-09-08	18:38:41	22:48:28	i'	45	320	2.203	0.216	2457640.353797	0.000241
WASP-69	T100	2016-10-09	17:30:55	21:45:34	R	90	105	0.810	0.497	2457671.298629	0.000301
WASP-69	T100	2017-08-26	18:23:04	22:57:27	I	100	103	0.484	0.826	2457992.354849	0.000199
WASP-69	T35	2019-07-27	20:27:08	01:26:27	R	30	511	5.495	0.437	2458692.486662	0.000519
WASP-69	T35	2019-08-27	19:20:50	00:25:27	R	20	732	6.326	0.110	2458723.431989	0.000381
WASP-74	T35	2019-07-07[c]	21:09:03	0 0:34:41	R	90	131	1.869	0.348	2458672.437582	0.000834
WASP-74	T100	2020-08-12	18:39:19	22:14:41	R	120	75	6.341	0.428	2459074.330869	0.000479
WASP-74	IST60	2020-08-14[a]	21:07:20	01:19:39	R	150	95	0.677	0.953	2459076.465929	0.000999
WASP-74	T100	2020-08-27	17:42:37	21:15:55	R	120	74	2.697	0.519	2459089.297844	0.000815
HAT-P-56	T35	2019-02-17	17:06:25	22:08:35	R	45	359	4.334	0.450	2458532.312128	0.001577
HAT-P-56	T100	2019-11-09	20:49:28	01:02:04	R	90	103	0.458	0.470	2458797.442744	0.000556
WASP-2	T35	2019-07-20	19:54:21	01:38:04	R	40	492	10.709	0.475	2458685.509228	0.001260
WASP-2	ATA50	2020-10-12	17:00:41	21:11:19	R	120	109	1.573	0.412	2459135.323994	0.000610
WASP-2	T100	2020-10-25	15:58:10	19:01:51	R	120	63	1.202	1.228	2459148.237230	0.000464
WASP-14	T35	2019-07-03	19:14:08	23:26:15	R	45	267	6.594	0.188	2458668.396037	0.001491
WASP-14	ATA50	2020-05-14[c]	17:24:45	20:30:34	R	20	307	1.635	0.548	2458980.286843	0.000612
HAT-P-32	T35	2019-11-03	16:45:39	02:57:18	R	100	297	1.240	0.504	2458791.414706	0.000351
WASP-103	T100	2014-05-30	22:48:14	01:48:47	R	145	53	0.542	0.863	2456808.530535	0.000296
WASP-103	CAHA	2015-04-30	23:56:16	04:16:09	R_c	145	106	0.380	0.650	2457143.577475	0.000183
WASP-103	CAHA	2015-06-07	20:24:31	01:58:08	I_c	90	183	0.694	0.898	2457181.524650	0.000241
WASP-103	T100	2017-06-11	19:42:54	01:37:55	R	130	117	1.077	0.553	2457916.407767	0.000683
WASP-103	T35	2018-07-01	19:40:25	00:04:00	Clear	60	187	1.053	2.313	2458301.434320	0.000447
WASP-103	T100	2020-07-29	19:02:37	22:38:46	R	120	75	0.983	0.318	2459060.382613	0.000595
HAT-P-37	T100	2015-08-04	21:30:11	01:56:51	R	150	79	0.712	0.818	2458532.312128	0.001577
HAT-P-37	T100	2019-05-17	19:45:14	00:53:57	R	115	139	0.832	0.526	2458621.418178	0.000250

[a]Eliminated because it is an outlier on TTV diagram.
[b]Eliminated because its depth is out of 3σ of the average.
[c]Eliminated because it is incomplete.

reveal the potential trends in the transit timings and understand their causes. Therefore, not all available transit light curves should be used prior to careful and quantitative inspection. Otherwise, it might lead to incorrect interpretations due to the lack of required data quality. Two well-defined metrics are widely used to quantify the quality of transit light curves in the literature. Photometric noise rate (PNR) (Fulton et al. 2011) is a primary indicator of the white noise although it is also affected by the red-noise component but to a lesser extent, and the β factor quantifies the red (or correlated) noise (Winn et al. 2008). We computed both metrics for each of the light curves we made use of, after checking the timings of observations carefully and converting the light curves given in the timing frames other than BJD–TDB. We employed a simple PYTHON code for measurements based on the definitions of these two metrics given in respective publications and previously used in our study of the HAT-P-19 system (Baştürk et al. 2020). However, we have found out that low-quality light curves leading to incorrect mid-transit timings can survive the thresholds based on these two metrics, especially the one that is based on the PNR. Therefore, we decided to follow the procedure we outline in the selection of light curves for analysis in this section.

First of all, we visually inspected all the available light curves in open data bases, in the literature, as well as our own. On the basis of this visual inspection, we eliminated the obviously problematic cases as a result, including all the incomplete ones since the timing of a mid-transit heavily depends on the timings of the ingress and the egress. We then checked if the noise level is comparable to the transit depth, making it difficult to achieve a model consistent with the properties of the system and to measure an accurate and precise mid-transit time as a result. We made use of PNR for the purpose, and if a light curve has a PNR value larger than or equal to the transit depth, we eliminated it. This ensured that we eliminated the lowest quality light curves but kept those that would help secure the sampling, especially in time intervals where there are not many observations although their error bars will also be large.

We also empirically determined a β factor of 2.5 to exclude the red noise-dominated light curves from our analysis. Moreover, the depths of the light curves have been taken into consideration making use of the model output value δ. We discarded the light curves with transit depths outside the 3σ of the weighted average transit depth of the light curves of a given system in a given passband.

Finally, we discarded the outliers in the final TTV diagrams based on two-tailed 3σ deviations from a simple linear fit with least-squares minimization. At the end of the entire selection procedure, 150 light curves have been eliminated out of 550, leaving 399 light curves behind for TTV analysis. We relaxed the final criterion for WASP-69 because, otherwise, only one data point, its first-ever transit observation published by Anderson et al. (2014), would be eliminated, despite the fact that it is very precise, leaving a large gap of almost 4 yr (∼1412 d) without a transit observation after it. The other transit observation published in the same study was also eliminated because it does not meet the depth criterion whereas the transit parameters derived from this first light curve are in very good agreement with that from all the other light curves analysed in this study. As a result, if we had not relaxed this criterion, the linear model's ability to correct its ephemeris would have been heavily influenced by more recent observations of lower quality.

Each of the light curves of a given system that survived the visual inspection was assigned a four-digit binary code composed of 1 s corresponding to the elimination due to the selection criterion in the order and 0 s to that survived from the same criterion. The first digit is for the β factor, the second for the PNR to transit depth ratio, the third for the transit depth (δ) as a sanity check for the transit, and the fourth for the outliers in the TTV diagram. If a light curve meets the selection criterion, then the corresponding digit to that specific criterion is assigned a value 0, or else 1 is assigned to indicate that it has been eliminated by our light-curve selection procedure. These four-digit binary codes for each of the light curves in our sample have been given in the data files corresponding to each of the systems. These digital binary codes and all the statistics employed in light-curve selection are provided in data files as the online supplementary material. We also provide the mid-transit times reported by observers as well as our own measurements of them from the same light curves together with their errors and the passband of the observations in those data files.

3 DATA ANALYSIS AND RESULTS

3.1 Light-curve modelling and measurements of mid-transit times

In order to measure the timing of the transit centre and to ensure the reliability of a selected light curve, we modelled it in EXOFAST (Eastman, Gaudi & Agol 2013). We preferred the first version of the code (EXOFAST-v1) running on a browser through the NASA Exoplanet Archive service to have homogeneous measurements of mid-transit times based on the same planetary and stellar parameters from the NASA Exoplanet Archive as well as speed and consistency in terms of CPU hours. This also makes the measurements more consistent for larger groups of researchers since all the collaborators work on the same parameter sets. We provided the priors for the linear and quadratic limb-darkening coefficients ourselves based on the passband of the observation and the fundamental parameters of the host stars after interpolations in the tables from Claret & Bloemen (2011) using the online tool provided by the EXOFAST website[4] (Eastman et al. 2013). We selected the *CoRoT* passband for light curves obtained without the use of a filter and the *R* band for the ones obtained with an R_c filter, because the transmission curves are similar.

[4]http://astroutils.astronomy.ohio-state.edu/exofast/limbdark.shtml

Prior to the analysis of the literature and data base light curves obtained by professional and amateur observers, we converted the timings of all observations from the timing reference frames they were recorded in to BJD–TDB by using our scripts that we developed based on the relevant modules and functions of the *astropy* package (Astropy Collaboration 2013, 2018). We also calculated the airmass values, using the same code to normalize and detrend the light curves that were not detrended for the effect. We made use of the AIJ software package for detrending, removing the obvious outliers, and reducing the raw data when necessary. Since all our light curves were detrended and normalized before the analysis as a result, we adjusted all the parameters, ran the EXOFAST-v1 code, and recorded all the results of the least-squares fit that it performed.

We used the output values of the models and their uncertainties for the transit depth (δ) and the mid-transit time error as well as the goodness of fit included in the computation of the PNR and the β factor, which are based on the EXOFAST-v1 model for the second level of light-curve elimination. Mid-transit times and their uncertainties of the light curves that survived also in this second phase of light-curve selection were used in our TTV studies. Since we had also taken the mid-transit timings and their uncertainties as reported by observers in open data bases and literature, we were able to compare our results at the end. This comparison allowed us to find the inconsistencies, such as incorrectly reported values by the observers as a result of modelling errors, references to incorrect timing frames (e.g. heliocentric Julian days instead of geocentric Julian days, in which the original measurements were made), and conversion errors between the timing frames and units. Where such inconsistencies were found, we contacted the observers, made sure of their source, asked for the raw data in critical cases, and repeated the measurements. Nevertheless, discrepancies between our and the observers' measurements and their uncertainties were expected although they were made on the same light curves because different software packages and methods have been allocated to derive the reported mid-transit times by the observers. Our measurements for all available light curves provide homogeneous sets of timing data. We discuss the discrepancies in more detail in Section 3.3.2.

3.2 Ephemeris corrections

In order to update the reference mid-transit times (T_0) and the orbital periods ($P_{\rm orb}$), we used EMCEE (Foreman-Mackey et al. 2013), a widely used Markov Chain Monte Carlo sampler, and created posterior probability distributions of the linear coefficients; slope for the correction term of the orbital period ($\Delta P_{\rm orb}$); and y-intercept for the correction term of the reference mid-transit time (ΔT_0). We assumed Gaussian priors centred at zero for an unbiased fit. The posterior distributions are then calculated by making use of the Gaussian priors and the likelihoods of the random normal samples, where the noise of the measurements is assumed to be independent and identically distributed as random normal variables with zero mean and constant variance. The correction terms for the reference mid-transit time and the orbital period were obtained from the median values of the posterior probability distributions, which we provide in Appendix B for all the planets in our sample (Figs. B1–B10). In all computations, the first 500 steps (the so-called burn-in period) were discarded in each of the random walkers until an equilibrium is settled. As a result, we corrected the ephemeris information for all the planets in our sample and listed reference values in Table 4 together with their uncertainties. Results have shown that the maximum uncertainty on a reference mid-transit time is 16.85 s and that on the orbital period is 0.10 s (for HAT-P-56 b). We should

Table 4. Reference ephemeris information (T_0 and P_{orb}).

Planet	T_0 BJD-TDB	P_{orb} (days)
HAT-P-23 b	2456539.390497(040)	1.21288643(004)
WASP-37 b	2458225.646784(161)	3.57747771(067)
WASP-69 b	2455845.538739(142)	3.86813577(032)
WASP-74 b	2457218.764573(056)	2.13775148(015)
HAT-P-56 b	2458822.558285(195)	2.79082643(116)
WASP-2 b	2456823.839482(062)	2.15222214(008)
WASP-14 b	2455632.578654(103)	2.24376644(022)
HAT-P-32 b	2454424.747289(055)	2.15000831(005)
WASP-103 b	2457511.944555(016)	0.92554549(003)
HAT-P-37 b	2457625.530538(056)	2.79744121(015)

point out here that we followed the same probabilistic approach in fitting quadratic functions to the TTV diagrams as well.

3.3 Transit timing analyses

We prepared TTV diagrams of all the planets in our sample by plotting the residuals of the observed mid-transit times from that calculated based on the corrected ephemeris information with respect to the epoch of observation (Fig. 1). We provided both our own measurements from all the selected light curves, colour coded according to the type of observation, and the reported values of these timings by the observers (in light grey) in order to show how homogeneous measurements make a difference. We detail the TTV analysis we performed for each of these systems in the forthcoming subsections.

3.3.1 HAT-P-23 system

HAT-P-23 b is a massive exoplanet ($M_p = 2.090 \pm 0.111 M_{jup}$) with an inflated radius ($R_p = 1.368 \pm 0.090 R_{jup}$) discovered by Bakos et al. (2011) at a short period ($P_{orb} = 1.212884 \pm 0.000002$ d). Moutou et al. (2011) determined that the orbit is aligned ($\lambda = +15^\circ \pm 22^\circ$) from Rossiter–McLaughlin observations, and O'Rourke et al. (2014) found that it is also circular from Spitzer observations of an occultation. Because an orbital decay is expected on the basis of its parameters, Maciejewski et al. (2018) and later Patra et al. (2020) studied its transit timings and updated the lower limit of the reduced tidal quality factor for the star to $Q'_\star > 5.6 \times 10^5$ and $Q'_\star > 6.4 \pm 1.9 \times 10^5$, respectively, both in 95 per cent confidence levels.

Our light-curve selection procedure ended up with 73 mid-transit times spanning 11.96 yr (3601 orbits in total), of which 33 are from amateur observers, 37 are from published light curves in the literature, and three from our own light curves. 12 light curves that we selected after our visual inspection of all the available light curves have been eliminated due to not being able to meet our quantitative selection criteria.

Relatively smaller discrepancies between the mid-transit times that we measure from a light curve and that reported by the observer should be expected. However, for a total of 10 points, the discrepancies are large enough to look for their sources. Therefore we contacted the observers and found that all 10 cases have been caused by reporting in a different timing reference than the original measurements were made in. The quality light curves published by Ciceri et al. (2015) constitute an especially interesting group, which can be seen at and around BJD-TDB 2456500. We contacted the authors of this study and found out that the reported timings have been converted into BJD–TDB twice, once for the entire light curves and the second time for the mid-transit times measured from them. When we corrected the timings, we had similar values, differing only by a few seconds at most. Nevertheless, we gave these timings as they were reported in order to point at potential problems that should be taken into account in a TTV analysis and for consistency.

The residuals of the linear fit to the TTV diagram have a full range less than ∼10 min, which is significant considering the error bars of the measurements. Therefore, we performed a frequency analysis with a PYTHON code based on the *astropy* function that computes Lomb–Scargle periodograms for time series data. Since the frequency with the maximum power in the periodogram has a false alarm probability (FAP) value of 61.4 per cent, we concluded that within the range and frequency of our observations there is no statistically significant periodicity in the TTV diagram. We then fitted the timing data with a quadratic function and compared the results with that from the linear fit with the differences in Bayesian Information Criterion (ΔBIC) and Akaike Information Criterion (ΔAIC). The linear model turned out to be more successful in representing the data in both statistics. Even if the second-degree polynomial was found to be superior, its quadratic coefficient would be positive within almost 2σ (1.92 to be exact). Therefore, the fifth percentile of the posterior probability distribution of the quadratic coefficient cannot be used to constrain a lower limit for $Q'_\star$. Instead, we provide the lower limit as $Q'_\star > 3.8 \times 10^6$ in 99 per cent confidence level. As a result, it can be asserted that there is no periodic or secular change in the transit timings of HAT-P-23 b within the limits of the observing window, the frequency of high-quality photometric observations, and observational uncertainties.

3.3.2 Comparison between heterogeneous and homogeneous measurements

There are multiple sources of errors in a TTV analysis due to the usage of inhomogeneous data sets from measurements made by different techniques and software packages giving different results and error estimates to inadequacies in timing of observations and reporting the results in different timing frames. In order to understand their consequences, we compared two data sets composed of the mid-transit times and their uncertainties as reported by the observers who published these timings either in open data bases or in refereed publications and that as measured by ourselves from the same light curves after validating the timing of observations.

First, we plotted the differences between mid-transit times, measured within this study and measured by the observers themselves who reported the values, with respect to the averages of both mid-transit time measurements (Fig. 2). We selected HAT-P-23 b as a sample case to explain our methodology because we have sufficient number of points for such an analysis. The median difference for the transit measurements of HAT-P-23 b indicated a positive bias between the two measurement sets, meaning that our measurements of the mid-transit times are ∼11 s larger compared to the reported values of the mid-transit times by the observers. The value of the median absolute deviation (MAD) of the differences (19 s), however, shows that the positive bias is not statistically significant. Since the mid-transit times reported by Ciceri et al. (2015) are found to be consistently smaller due to an error in their conversion to BJD-TDB, we excluded these measurements and repeated the analysis and found a better agreement between the measurements with a median difference of ∼8 s and a MAD of 28 s. This time three mid-transit times reported to the Exoplanet Transit Database (ETD) affected the

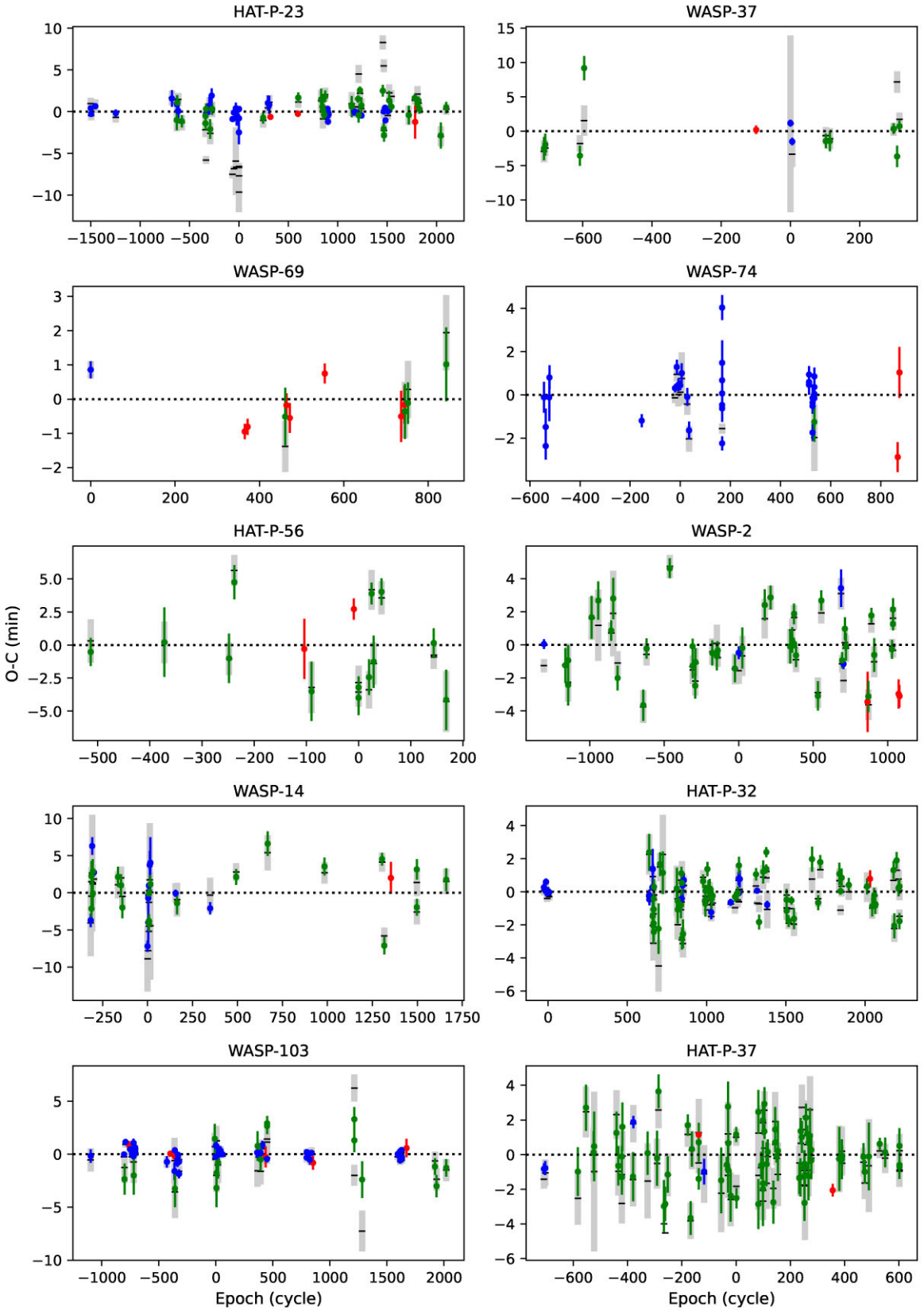

Figure 1. TTV diagrams for all the planets in our sample based on observations from open data bases (green), our observations (red), and light curves published in the literature (blue). The mid-transit times reported by the observers are shown in grey for comparison for the same light curves except our own.

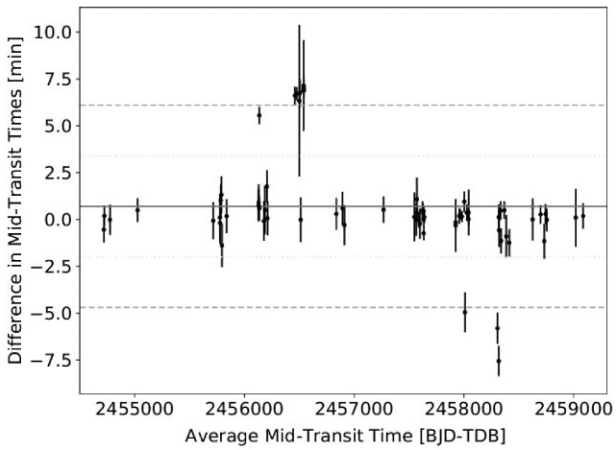

Figure 2. Differences between the mid-transit times measured from EXOFAST-v1 models for this study and that reported by the observers with respect to the average of both measurements for HAT-P-23. Sources of both the positive and negative outliers are provided in the text.

Table 5. Comparison of the observers and our own measurements of the mid-transit times. Details of the comparison statistics are provided in the text.

System name	Range of O–C our & obs. (min)	$\sigma_{\text{O–C}}$ our & obs. (min)	Median diff. ± MAD (s)
HAT-P-23	5.42 & 15.69	1.11 & 2.92	8 ± 28
WASP-37	12.84 & 6.38	3.40 & 1.87	7 ± 78
WASP-69	2.82 & 3.55	0.93 & 1.42	−3 ± 38
WASP-74	6.90 & 15.36	1.29 & 3.50	27 ± 24
HAT-P-56	8.92 & 8.11	2.89 & 3.27	2 ± 37
WASP-2	8.29 & 8.88	1.98 & 1.78	12 ± 26
WASP-14	13.82 & 14.15	3.39 & 3.60	44 ± 72
HAT-P-32	5.28 & 5.38	1.22 & 1.06	17 ± 18
WASP-103	6.63 & 13.49	1.17 & 1.43	9 ± 11
HAT-P-37	7.31 & 7.28	1.53 & 1.66	14 ± 47

magnitude of the bias considerably. We corrected the timings from Ciceri et al. (2015); however, we were unable to find the sources of the deviations of three mid-transit times reported to the ETD. Since they were not eliminated by our light-curve selection algorithm, we analysed them based on the measurements from our model. We followed the same procedure for all the planets in comparison of the observer measurements and our own measurements of the mid-transit times. We provide the median of the differences and the corresponding MAD statistics in Table 5 as well as the range and standard deviation of TTVs formed by two data sets for comparison, which are smaller for our measurements than the observer-reported values owing to our homogeneous analysis approach. This reduction of the scatter in data is illustrated in Fig. 3 for HAT-P-23 b. Although median differences and associated MAD values do not indicate any disagreement between two sets of measurements, homogeneous measurements may help to recover potential periodicities with a better SNR since biases between measurement and data analysis techniques are avoided. Moreover, the advantage of working on a homogeneous set of measurements will be clearer for larger sets, and the comparisons with the original measurements will be fair. Consequently, we based our TTV analysis on our own measurements for the rest of this study.

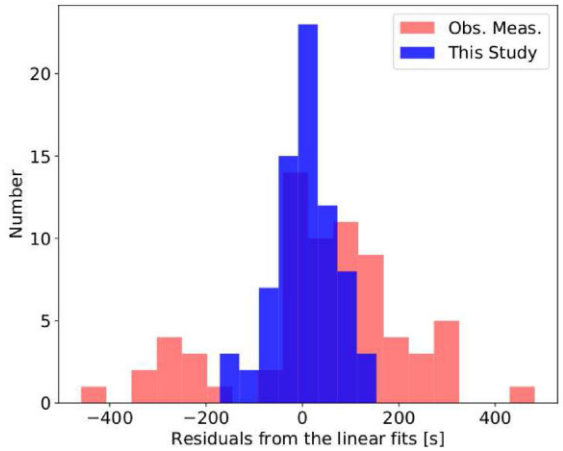

Figure 3. Histograms of the residuals from the linear fits to our measurements of the mid-transit times (this study, in blue) and the reported values of mid-transits (observers' measurements, in red) for HAT-P-23.

3.3.3 WASP-37 system

Simpson et al. (2011) discovered the transiting planet WASP-37 b orbiting an old (11^{+3}_{-4} Gyr), metal-poor star. They noted that if the reduced tidal quality factor is $Q'_\star > 10^7$, then the planetary spiral-in time-scale should be longer than the main-sequence lifetime. They also argued that the planet has a larger radius than it should have, based on the extent of the expected photo-evaporation from its age. Mallonn et al. (2019) analysed the transit timings of the planet accumulated until the time of their study and corrected the linear ephemeris as a result.

We analysed 11 transit light curves of WASP-37 b downloaded from open data bases, two light curves from the literature (Mallonn et al. 2019), one UT50, and two T100 light curves (one of which is incomplete), adding up to a total of 15 light curves. Two more light curves were excluded after the second stage of the light-curve selection procedure. As a result, 12 light curves formed the TTV diagram with a baseline of 10.06 yr of observations. Although the observations form a sufficiently long baseline for a TTV analysis, the overall number of light curves is small. Therefore, we attempted only at linear and linear + quadratic models of our measurements, the former of which was found to be superior to the latter in terms of ΔBIC and ΔAIC values. Consequently, we corrected the ephemeris information based on the parameters of the linear fit. The residuals from the linear fit are scattered within a range of ∼5 min if the literature minimum deviating from the linear trend by more than 10 min is ignored. More observations will be needed to clarify if the scatter is indicative of a real variation.

3.3.4 WASP-69 system

WASP-69 b is a Saturn-mass planet with an inflated atmosphere, orbiting a young (∼1 Gyr) and magnetically active K-star in 3.868 d. It was discovered by Anderson et al. (2014), who obtained a global model of the transit and RV measurements after removing the spot-induced modulations on the light curves. They found that the eccentricity term in the RVs did not improve the results and so adopted a zero-eccentricity for the orbit. This was later confirmed by Wallack et al. (2019) based on Spitzer occultation observations. Since WASP-69 b has an inflated atmosphere and is orbiting an active star, mass loss has been predicted due to evaporation driven by high-energy particles (Anderson et al. 2014). Finally, Nortmann et al.

(2018) detected excess absorption in the helium triplet at 1083 nm during a transit of WASP-69 b, which they interpreted as the escape of part of the atmosphere trailing behind the planet in comet-like form. Vissapragada et al. (2020) confirmed their finding and constrained the mass loss rate to be $5.25^{+0.65}_{-0.46} \times 10^{-0.4} M_{\rm jup}$ per Gyr from their ultra-narrow band observations of a transit of WASP-69 b.

WASP-69 b is an overlooked planet in terms of ground-based transit observations. Only five transit light curves were found in the open data bases of sufficient quality. The two published light curves are from the discovery study by Anderson et al. (2014). We observed the target twice with AUKR's T35 in order to make sure about the ephemeris information for the transit observations. In addition, we have three precise light curves from CAHA 1.23-m telescope, and two from the T100, which enabled us to form a TTV diagram covering 8.93 yr. One of the light curves from Anderson et al. (2014) was eliminated from our study since it does not meet the transit depth criterion. Consequently, the TTV diagram for WASP-69 b is based on 13 light curves. The linear + quadratic model to our measurements performs better than the linear model based on the ΔBIC and ΔAIC values. However, there is a large gap between the first transit observation of the target, which is above the best-fitting line, and the second observation. It is difficult to detect a secular change in the orbital period based on a data set of only 13 points, with a gap of more than 350 epochs. As a result, we corrected only the ephemeris of WASP-69 b, which will be targeted for further analysis of its inflated atmosphere in future ground-based and space-borne observations. The residuals of the linear fit have a scatter of less than 4 min, which is statistically significant when the measurement uncertainties are taken into account. In order to understand this potential variation, more observations are needed.

3.3.5 WASP-74 system

WASP-74 b was discovered by the SuperWASP team (Hellier et al. 2015) around a late F-type (F9), bright ($m_V = 9^m.7$), southern star. Mancini et al. (2019) analysed 18 light curves from 11 multicolour planetary transits of WASP-74 b, eight of which were obtained simultaneously in different filters in the NIR with the GROND instrument on MPG 2.2-m telescope in La Silla. They derived mid-transit times from the eight complete transits in their data set. They found the orbital period to be smaller by 0.475 s than the value in the discovery paper.

WASP-74 b was classified as an inflated hot Jupiter because its radius ($R_p = 1.56 \pm 0.06\ R_{\rm jup}$) is relatively large for its mass ($M_p = 0.95 \pm 0.06\ M_{\rm jup}$) (Hellier et al. 2015). However, the distance of the star was found to be $d = 120 \pm 20$ pc from its global modelling by Hellier et al. (2015), whereas the *Gaia* parallax (Gaia Collaboration 2016, 2018) gives a distance of $d = 148.029 \pm 1.037$ pc (after correction for the systematic offset noticed by Stassun & Torres 2018). The small uncertainty in the *Gaia* parallax prompted us to refine the parameters of WASP-74 based on a global model of the best light curves in our data sets, published and unpublished RVs from 29 archival HARPS spectra acquired in two different nights, and the directly measured distance from *Gaia*. Garhart et al. (2020) confirmed that the orbit is circular through Spitzer occultation observations, so we fixed the eccentricity to zero.

We collected broad-band photometric magnitudes from 2MASS (Skrutskie et al. 2006), WISE (Wright et al. 2010), Tycho-2 (Høg et al. 2000), SDSS (Alam et al. 2015), and APASS (Henden et al. 2015) catalogues (listed in Table 6), and fitted the spectral energy distribution (SED) of WASP-74 using the second version of EXOFAST (Eastman et al. 2019). We employed the atmospheric parameters ($T_{\rm eff}$, log g, and [Fe/H]) obtained by Sousa et al. (2018) as Gaussian priors with widths equal to their uncertainties. The effective wavelengths of the broad-band photometry passbands were gathered from the Spanish Virtual Observatory Filter Service (Rodrigo, Solano & Bayo 2012; Rodrigo & Solano 2013). Finally, we limited the extinction value using the dust maps published by Schlegel, Finkbeiner & Davis (1998). We calculated the radius of the star $R_\star$ from our SED fit and provided its value as a Gaussian prior for the global modelling during which we fit the RV measurements, transit light curves, and stellar-isochrone tracks. Instead of using the uncertainty on $R_\star$ derived from the SED fitting, which is below the systematics in their calibration, we made use of 3.5 per cent of the radius value as a Gaussian width for the global modelling. This systematic error floor comes from the precision of the interferometric angular diameters (White et al. 2018) and the disagreements in the measurements of bolometric fluxes between various methods (Zinn et al. 2019).

Table 6. Passband brightnesses of WASP-74.

Passsband	$\lambda_{\rm eff}$Å	Magnitude
Tycho-2 (Høg et al. 2000)		
B_T	4280.0	10.533 ± 0.042
V_T	5340.0	9.823 ± 0.033
APASS-DR9 (Henden et al. 2015)		
Johnson B	4378.1	10.388 ± 0.037
Johnson V	5466.1	9.731 ± 0.037
SDSS g'	4640.4	10.102 ± 0.066
SDSS (Alam et al. 2015)		
SDSS i'	7439.5	9.432 ± 0.002
2MASS (Skrutskie et al. 2006)		
J	12350.0	8.548 ± 0.037
H	16620.0	8.286 ± 0.018
K_S	21590.0	8.221 ± 0.023
All WISE (Wright et al. 2010)		
WISE1	33526.0	8.119 ± 0.023
WISE2	46028.0	8.178 ± 0.019
WISE3	115608.0	8.187 ± 0.021
WISE4	220883.0	8.160 ± 0.267

We added six new data points to the RV curve of WASP-74 from archival HARPS observations. There are 29 spectra recorded in two consecutive nights (2017 August 17 and 18) in the HARPS public archive lacking RV measurements. We downloaded the 1D-spectra reduced and corrected for the Earth's orbital motion by the HARPS pipeline. We normalized them to the continuum level with the latest version of the iSpec software package for spectral analysis (Blanco-Cuaresma et al. 2014; Blanco-Cuaresma 2019), making use of a synthetic spectrum as a visual template, that we created with the relevant tools of the same package based on the fundamental parameters of the star from Sousa et al. (2018). Then, we measured the RVs by cross-correlating the observed spectra corrected for the orbital motion of the Earth with the spectral mask from the HARPS pipeline created for G2 stars. We binned the resultant RVs to form three data points for each of the nights in order to avoid the intra-night jitter after a few attempts with different amounts of binning. We provide the individual measurements and the RV values after binning within the online materials. There is an offset between the CORALIE and HARPS RVs either due to an instrumental offset or a change in a longer time-scale than the baseline of each of the data

Table 7. Parameters of the global model for WASP-74 system and their 1σ error bars from EXOFAST-v2 compared to those from Hellier et al. (2015) (H2015).

Parameter (unit)	Value	H2015
Stellar parameters:		
$M_\star$ ($M_\odot$)	$1.316^{+0.052}_{-0.053}$	1.48 ± 0.12
$R_\star$ ($R_\odot$)	$1.578^{+0.024}_{-0.025}$	1.64 ± 0.05
$L_\star$ ($L_\odot$)	3.03 ± 0.14	–
$\rho_\star$ (cgs)	0.472 ± 0.011	0.338 ± 0.018
$\log g$ (cgs)	$4.1608^{+0.0088}_{-0.0091}$	4.180 ± 0.018
$T_{\rm eff}$ (K)	6064 ± 42	5990 ± 110
[Fe/H] (dex)	$+0.465^{+0.026}_{-0.027}$	$+0.39 \pm 0.13$
Age (Gyr)	$3.43^{+1.00}_{-0.82}$	–
$A_{\rm V}$ (mag)	$0.215^{+0.052}_{-0.051}$	–
d (pc)	$148.2^{+1.9}_{-1.8}$	120 ± 20
Planetary parameters:		
$P_{\rm orb}$ (days)	$2.13775132^{+0.00000053}_{-0.00000055}$	2.137750 ± 0.000001
$T_{\rm C}$ (BJD − TDB)	$2457173.871443 \pm 0.000080$	–
$R_{\rm P}$ ($R_{\rm J}$)	$1.407^{+0.023}_{-0.024}$	1.56 ± 0.06
$M_{\rm P}$ ($M_{\rm J}$)	$0.877^{+0.037}_{-0.038}$	0.95 ± 0.06
a (AU)	$0.03559^{+0.00046}_{-0.00049}$	0.037 ± 0.001
i (degrees)	$79.95^{+0.12}_{-0.11}$	79.81 ± 0.24
e	0.00 (fixed)	0.00 (adopted)
K (m/s)	113.5 ± 3.7	114.1 ± 1.4
$T_{\rm eq}$ (K)	1947 ± 16	1910 ± 40
Transit parameters:		
b	$0.8460^{+0.0031}_{-0.0033}$	0.860 ± 0.006
δ (fraction)	0.008393 ± 0.000051	0.00961 ± 0.00014
a/R_*	$4.849^{+0.038}_{-0.037}$	–
τ (days)	0.02574 ± 0.00055	0.0288 ± 0.0014
T_{14} (days)	$0.09865^{+0.00038}_{-0.00037}$	0.0955 ± 0.0008
RV Parameters:		
	CORALIE	HARPS
RV Offset (m/s)	$-15764.9^{+3.2}_{-3.1}$	$-15755.6^{+7.6}_{-7.5}$
RV Jitter (m/s)	$13.0^{+3.0}_{-2.3}$	$19.1^{+2.3}_{-3.1}$

sets. EXOFAST-v2 computes the RV of the barycentre of the system (V_γ) for both sets of measurements and corrects for the offset in the RV fit, which is only $9.3\ ^{+8.2}_{-8.1}$ m/s.

We selected only very precise and complete light curves from the literature and our own observations for global modelling. However, we used an incomplete light curve if it is the only one acquired in a certain passband for a wider wavelength coverage. That is why we included the RISE light curve observed in Johnson V band (2014 August 19) given by Hellier et al. (2015), and the GROND light curve in the K band (Mancini et al. 2019) although they are affected by the white noise to a larger extent (PNR > 3.0). We observed the target on five nights with different telescopes. However, the light curves we acquired with the 43-cm telescope in Observatoire des Baronnies Provençales (OBP43), the 60-cm telescope IST60 in our network, and two light curves obtained with T100 in TÜBİTAK National Observatory (T100) were either incomplete or affected by red noise. Hence, we decided to use the light curve acquired through a Bessell R filter with T100 on 20/08/12 in the global modelling. Consequently, we were able to model 15 precise light curves of the target simultaneously with 20 CORALIE and six HARPS RV measurements, which form the largest and most precise data set analysed so far in the literature for WASP-74.

We used EXOFAST-v2 (Eastman et al. 2019) for the global modelling of the light and RV curve data, fundamental atmospheric parameters derived from a detailed spectroscopic analysis by Sousa et al. (2018), and the brightness of the host star in different passbands. We enforced a Gaussian prior only on the orbital period ($P_{\rm orb}$ = 2.1377445 ± 0.0000018 d) determined by Mancini et al. (2019) with a width of its uncertainty. We assumed a circular orbit for the planet because the eccentricity was found to be smaller than 0.07 in 3σ, and the circularization time-scale is smaller than the age of the system (Hellier et al. 2015). The fundamental parameters of the stellar atmosphere and their uncertainties were taken from Sousa et al. (2018) and were assigned as Gaussion priors. The surface gravity was adjusted because light-curve modelling of transits constrains the parameter better than spectroscopy (Southworth, Wheatley & Sams 2007). The coefficients of the quadratic limb darkening law are interpolated from the tables by Claret & Bloemen (2011) during the light-curve fitting process. Orbital inclination (cos i) was assigned a uniform prior.

As a result, we achieved a global model that satisfactorily fits all the light curves in different passbands acquired with different telescopes and the RV curves from two spectrographs. We list the parameters of our global model in Table 7 and provide the light curves in Fig. 4 and the RV curve in Fig. 5 together with models based on those parameters.

TTV Analysis of WASP-74: After obtaining its global parameters, we analysed 42 transit light curves in total, including three light curves from open data bases, 23 from the literature (seven from Hellier et al. 2015), and 16 from Mancini et al. (2019), and 2 T100, 1 IST60, and 1 T35 light curves. 36 of these light curves survived the quantitive light-curve elimination and formed the TTV diagram with an observation baseline of 8.305 yr. We corrected the reference mid-transit time and the orbital period from a linear fit to this TTV diagram composed of our measurements of the mid-transit times. We did not find any evidence for either a quadratic or a periodic variation in the analysis of the TTV diagram of WASP-74 b.

3.3.6 HAT-P-56 system

Huang et al. (2015) detected the inflated and massive hot Jupiter-type planet HAT-P-56 b with the HATNet telescopes, later confirmed by *Kepler*/K2 observations. Since the transit is grazing, the uncertainty on the radius was found to be large because the transit depth is highly dependent on the limb-darkening parameters. The advantage of the large-impact parameter is that the timings of the transit will be measured within more precision thanks to the V-shape of the light curve, and hence the system has more potential to be studied in terms of its TTV and TDV. An interesting finding is that the rotation period of HAT-P-56 ($P_{\rm rot}$ = 1.98 ± 0.08 d) turned out to be shorter than the orbital period of the planet HAT-P-56 b ($P_{\rm orb}$ = 2.79 d) (Zhou et al. 2016), which is in agreement with the period derived from a strong peak at 1.744 ± 0.023 d in the periodogram of the long-cadence K2-light curve of the target and the spectroscopic projected rotational velocity (v sini = 40.1 km/s) found by Huang et al. (2015). This can be indicative of a weak tidal interaction between the star and the planet or the planet might have been pushed away by the tides from the star from an even closer orbit, which might also be detected in its TTVs.

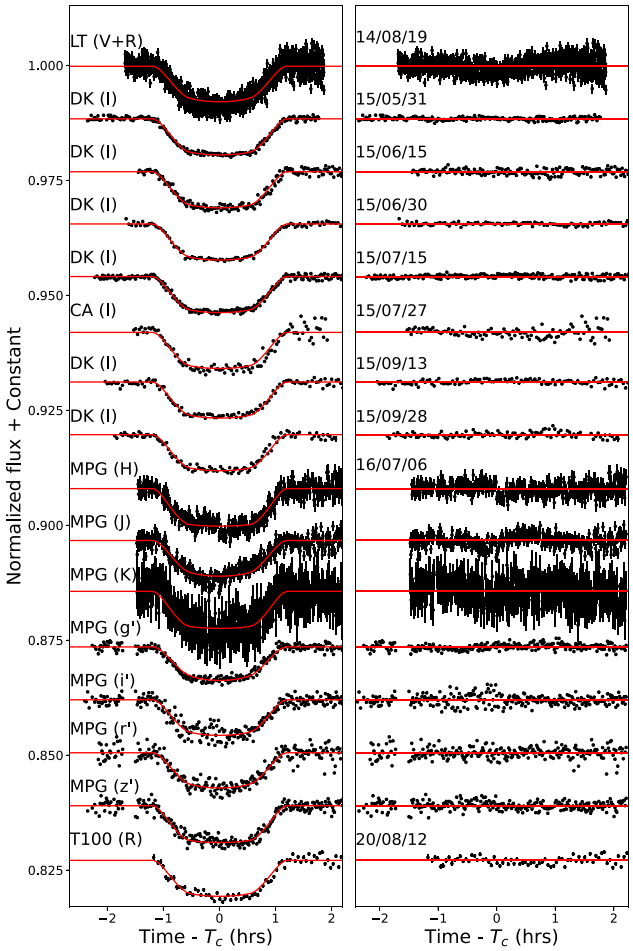

Figure 4. Individual transit observations of WASP-74 (black data points) and their EXOFAST-v2 models (red continuous curve) to each of these light curves based on the parameters in Table 7 (on left) and the residuals (on right). The telescope and the passband of observation are given on the upper left corner for each light curve. DK (1.54-m Danish Telescope at La Silla Observatory), CA (1.23-m telescope at CAHA), and MPG (2.2-m Max Planck Gesellschaft Telescope at La Silla Observator on 2016 July 6) light curves were obtained by Mancini et al. (2019); LT (2-m Liverpool Telescope at Roque de los Muchachos Observatory) light curve was published by Hellier et al. (2015); and T100 denotes 1-m Telescope at TUG (this study). Observation dates are given in YY/MM/DD format next to the residuals.

Only 18 transit light curves were found in open data bases for HAT-P-56 b. We observed the target with T35 and T100 in 2019. Unfortunately, the light curves published in the literature were not adequate in deriving reliable mid-transit times, and four of the 20 light curves we had were eliminated during our second stage of light-curve selection based on quantitative criteria. Therefore, the resultant TTV diagram was formed by only 16 data points in total, which can be best described with a linear model. We corrected the reference light elements as a result and listed them in Table 4. The residuals of this linear fit scatter within a full range of ∼10 min, which should be tracked with future transit observations of the target. Although the orbit was also found to be aligned ($\lambda = 7^{+2}_{-2}$ deg) by Zhou et al. (2016), the RVs of the system obtained to verify the planetary nature of the companion with TrES spectrograph can be modelled with a slight eccentricity ($e = 0.130 \pm 0.058$) (Huang et al. 2015), which strengthens its importance for future TTV studies.

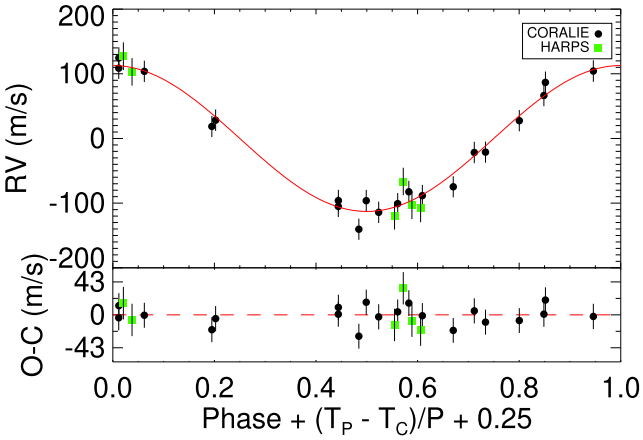

Figure 5. Radial velocity observations from CORALIE (Hellier et al. 2015) (black data points) and HARPS derived in this study (green data points) phased with the ephemeris information given in Table 4. The red curve represents our Keplerian model based on the parameters in Table 7. Residuals of the model are given in the lower panel.

3.3.7 WASP-2 system

WASP-2 b is the second planet discovered during the SuperWASP survey for transiting planets (Collier Cameron et al. 2007), orbiting its star in a retrograde orbit (projected angle is $\lambda = -153^{+15}_{-11}$ degrees) (Triaud et al. 2010). Daemgen et al. (2009) identified a nearby contaminating source in their Lucky Imaging survey. This potential stellar companion was studied several times (Bergfors et al. 2013; Ngo et al. 2015; Piskorz et al. 2015; Wöllert et al. 2015; Evans et al. 2016). VLT/SPHERE observations by Bohn et al. (2020) confirmed that this visual companion is comoving with the WASP-2 system. Southworth et al. (2020) corrected the RVs for this contamination and reanalysed the system and refined its parameters as a result. Addison et al. (2019) observed a transit of WASP-2 b with a high precision with MINERVA telescopes in the Sloan r' filter. Although they found a significantly smaller period, they did not attempt an explanation. Despite an expectation of an orbital decay from the system based on its parameters, Baluev et al. (2019) studied the TTV of the planet WASP-2 b and were able to fit the transit timings with an upward parabola implying an orbital period increase with $\frac{dP}{dn} = 3 - 10 \times 10^{-10}$ d per cycle. From their fit to previous RV observation, they found a deceleration of -3.9 m s^{-1} yr^{-1}. Their global fit to RV and TTV resulted in an slightly eccentric orbit ($e = 0.0134 \pm 0.0056$) with an orbital decay time-scale (linear time-scale of the orbital period to be zero) of $T_{\rm d} = \frac{1}{q} = \frac{P}{\dot{P}} = -12 \pm 11$ Myr. Non-zero eccentricity, which was assumed to be zero in all previous analyses, was also confirmed by Spitzer occultation observations (Wheatley et al. 2010).

We assembled 57 complete transit light curves of WASP-2 b, with sufficient quality for a TTV analysis. The open data bases have 50 transits, there is one from Addison et al. (2019),one from Turner et al. (2017), one from Charbonneau et al. (2007), one from Ignatov, Gorbachev & Shlyapnikov (2020), and three from our own observations (T35, ATA50, and T100). 47 of these light curves survived our second stage of the light-curve elimination procedure, forming the TTV diagram with a 14.07-yr baseline. Having corrected the TTV diagram with an updated ephemeris, we performed a frequency analysis using a Lomb–Scargle periodogram. We found a peak at 268.31 d, with a FAP of 38 per cent, which is not significant. We then attempted to fit the timings with a linear + quadratic model, which turned out to be inferior to the linear lit. However, an ∼10-min

range scatter, larger than the observational error bars, is observed in the residuals of the linear fit that we present in Fig. 1.

3.3.8 WASP-14 system

WASP-14 b is a dense planet ($\rho_p = 3.501$ g cm^{-3}) in a short-period ($P_{orb} \sim 2.24$ d), slightly eccentric ($e \sim 0.09$), and misaligned ($\lambda = +33^\circ.1 \pm 7^\circ.4$) orbit (Joshi et al. 2009). The eccentricity of the orbit was later confirmed based on the Spitzer measurements as $e = 0.087 \pm 0.002$ by Blecic et al. (2013). On the basis of its parameters and the fiducial values of tidal dissipation parameters for both the star and the planet from Jackson, Greenberg & Barnes (2008), Joshi et al. (2009) found that the time-scales of both circularization and decay of the orbital semimajor axis should be smaller than 1 Gyr. On the other hand, the age of the star was found to be between 0.5 and 1 Gyr, both from its lithium abundance and from stellar evolution models. Therefore, the WASP-14 system may be very close to the lower limit for the point at which orbital eccentricity can survive tidal evolution for a sufficiently long time. If this is not the case, and the reduced tidal quality factor is not large enough ($Q'_\star > 6.6 \times 10^6$) for the planet to survive on an eccentric orbit, then an unseen potential third body can explain the small but statistically significant eccentricity of the orbit. Ngo et al. (2015) detected a $0.33 \pm 0.04 M_\odot$ stellar companion to WASP-14 at a separation of 300 ± 20 au, which was later found to be an early-type background source from flux ratios by Wöllert et al. (2015). Raetz et al. (2015) provided the first TTV analysis of the system but found no significant periodic signal in their frequency analysis based on a 7-yr long baseline of observations including their own 19 light curves of 13 transit events. Nevertheless, they reported an orbital period 1.2 s longer and 10 times more precise than the previous value.

We analysed 39 transit light curves of WASP-14 b, 24 of which have been reported to the ETD, 13 of which appeared in the literature and two of which are our own observations with ATA50 and T35. 31 of these light curves were found to be of sufficient quality by our selection criteria. We attempted linear + quadratic fits to the data. Positive ΔBIC and ΔAIC values showed that the latter model was more successful in describing the data set formed by our own measurements. The case was the same for the data set composed of the reported values of the mid-transit times. The orbital period of WASP-14 b is not expected to increase because the time-scale for an orbital decay was found to be less than 1 Gyr, while the lithium abundance and the location of the host star on isochrones both give an age value between 0.5 and 1.0 Gyr (Joshi et al. 2009). However, the only other TTV analysis of the system by Raetz et al. (2015) also resulted in a larger orbital period than the previous value. On the other hand, the residuals from both linear and the linear + quadratic models have scatters larger than 15 min. Non-zero eccentricity increases the probability of the existence of an unseen third body on a larger orbit, which would explain both the eccentricity and the statistically significant TTV variation. Our analysis is based on only 31 precise and complete transit light curves spanning a baseline of 12.15 yr, which is an improvement on the data set that Raetz et al. (2015) used in their study. We searched for periodicity in the residuals of the linear fit with a Lomb–Scargle periodogram, finding the peak of maximum power to be at 59.06 d. However, its FAP is only 5 per cent and so is not sufficient to claim any periodicity.

3.3.9 HAT-P-32 system

HAT-P-32 b is orbiting a relatively young star (2.7 ± 0.08 Gyr), which is a magnetically active star manifested by its high RV jitter of over 80 m/s (Hartman et al. 2011). There has been dispute on the orbital eccentricity of the system in the past based on the RV models (Hartman et al. 2011; Gibson et al. 2013; Knutson et al. 2014); however, the orbital phase of the occultation observations by Spitzer revealed the circular nature of the orbit (Zhao et al. 2014). The linear trend found by Knutson et al. (2014) in the RV observations with a slope of -33 ± 10 m s^{-1} yr^{-1} was not found to be caused by the nearby companion detected by Adams et al. (2013) and later Zhao et al. (2014) from flux ratios in multiple visual and IR passbands. Seeliger et al. (2014) analysed all the precise transit timings of the system available at the time and ruled out TTV amplitudes larger than ~1.5 min. Wang et al. (2019) analysed more mid-transit times accumulated until the time of their study and reached the same conclusion.

We found 104 complete transit light curves of HAT-P-32 b in the open data bases (81) and the literature (22 in total from Hartman et al. 2011; Sada et al. 2012; Tregloan-Reed et al. 2018; Wang et al. 2019) and observed the target once with T35 to check the ephemeris information. Although HAT-P-32 was observed by TESS in Sector-18 (2019 November), the observations were in the long cadence (30 min), which is not adequate to acquire precise mid-transit timings. On the basis of our quantitative criteria, we selected 82 of the light curves in our sample. These are evenly distributed apart from a gap of 3.175 yr after the first few data points from the discovery paper (Hartman et al. 2011). A Lomb–Scargle periodogram has no peaks with a FAP smaller than 12 per cent, which is for an unrealistically small period of 23.71 d. We thus ruled out a periodicity in TTV within the limits of the data set and corrected only the ephemeris information for the system (Table 4). The residuals of the linear fit have a range of ~5 min.

3.3.10 WASP-103 system

Gillon et al. (2014) announced the discovery of the 'ultra' hot Jupiter WASP-103 b on a very short-period ($P_{orb} < 1$ d) orbit, larger than its Roche radius by only 20 per cent, making it a candidate for mass loss and eventual tidal disruption, hence a decrease in its orbital period. Wöllert & Brandner (2015) detected a nearby source at an angular distance of $0''.242 \pm 0''.0.016$ from WASP-103. Southworth & Evans (2016) reanalysed their light curves they presented in Southworth et al. (2015), characterized this visual companion, and found that its effect on the measured physical properties of the host star will be small. Cartier et al. (2017) derived the effective temperature of this visual companion as $T_{eff} = 4400 \pm 200$ K from their SED fitting for the visual companion, which is consistent with the results of Ngo et al. (2015), and that of Southworth et al. (2015), who reported a mass value of $0.72 \pm 0.08 M_\odot$ for this star. The system is not resolved by *Gaia* in either the DR2 or EDR3 data releases. Cartier et al. (2017) corrected their secondary eclipse observation for this companion and found that its timing was consistent with zero eccentricity. Turner et al. (2017) presented the first near-UV transits (Bessell *U*) of WASP-103 b and constructed a TTV plot with the data accumulated until the time of their study. However, they found no variation in its transit timings. Maciejewski et al. (2018) also studied the TTV diagram but did not find a variation other than the linear ephemeris suggested. They constrained the reduced tidal quality factor (Q' to be larger than 10^6 at 3.5σ confidence). Delrez et al. (2018) analysed new and precise transit and occultation light curves and RV data and found consistent results with the previous findings. Patra et al. (2020) studied the TTV of the system based on the most precise light curves of the target and four light curves they acquired with the 1.2 m telescope at the Fred Lawrence Whipple Observatory (FLWO). Their best-fitting orbital decay model resulted in a positive period change. They constrained

the reduced tidal quality factor to be $Q' > (1.1 \pm 0.1) \times 10^5$ with 95 per cent confidence as a result, contradicting the previous findings and potential mass loss expected from the nature of the planet. Most recently, Barros et al. (2022) also found an increase in the orbital period based on their data set extended by their own observations with CHEOPS as well as re-reduced *HST* and Spitzer data. However, their quadratic model is not statistically superior to the linear model.

WASP-103 b is a frequently studied planet owing to its very short period ($P < 1$ d), leading to an expectation of a decay in its orbit. We observed the transits of the planet in high precision with 1-m T100 three times, and 1.23-m telescope of CAHA twice in addition to an observation with T35 with inferior quality. We collected 55 precise light curves from the literature, including 14 from Southworth et al. (2015), the TRAPPIST light curve from Gillon et al. (2014), three from Lendl et al. (2017), one light curve from Turner et al. (2017), two from Delrez et al. (2018), eight in total from Maciejewski et al. (2018), four from Patra et al. (2020), 10 very precise light curves obtained with different instruments to form a transmission spectrum of WASP-103 b from Kirk et al. (2021), and most recently 12 light curves from Barros et al. (2022), four of which we had to eliminate due to insufficient sampling for timing analysis. We found 22 complete light curves in the ETD, five of which were eliminated by our selection criteria. We continued our analysis with our measurements of the conjunction times of 75 light curves selected after our second stage of the selection procedure spanning 7.90 yr. The linear model turned out to be superior to the linear + quadratic model, the quadratic term of which is found to be negative. However, until the time of the recent publication of very precise transit observations of WASP-103 b by Kirk et al. (2021), the trend that was observed in the TTV was an upward parabola as found by Patra et al. (2020) and Barros et al. (2022), which lacks the data from Kirk et al. (2021) in their analysis, in contrast of the expectation of an orbital decay from the ultra-short period. These observations seem to have changed the picture and showed the need for further precise observations of the target to reveal its orbital period behaviour. Nevertheless, we determined a lower limit for $Q'_\star$ as $>1.4 \times 10^6$. Although it is difficult to argue for a period change in its TTVs with only 75 data points, a peak at frequency corresponding to a periodicity of 76.15 d was found with a FAP value of 1.63 per cent in its Lomb–Scargle periodogram, which we note for future observations of the target with a reservation that it probably arises from seasonal sampling.

3.3.11 HAT-P-37 system

HAT-P-37 b is a hot Jupiter discovered in the HAT-Net survey by Bakos et al. (2012). Maciejewski et al. (2016) published two complete and two incomplete transit light curves of the target. They analysed them and obtained similar results to Bakos et al. (2012). They computed the mid-transit timings of their own light curves together with that of Bakos et al. (2012), constructed the TTV diagram, and corrected the ephemeris information from a linear fit for the uncertainties on reference light elements. Then, Turner et al. (2017) observed the system in Harris B and R filters on 2015 July 1. They found a difference in $R_P/R_\star$ between the values they derived from the transit depths in B and R bands by 2.6 σ, which could be indicative of a TiO/VO absorption in its atmosphere.

We analysed 91 transit light curves of HAT-P-37 b. Four of these light curves are from the literature (Bakos et al. 2011; Maciejewski et al. 2018), 85 are from ETD, and two are from our own high-precision observations with T100. TESS has also observed HAT-P-37 in both long cadence and short cadence, but these data are affected by a star 29″.62 with large intrinsic variability. The two sources cannot be resolved by TESS and have different distances from *Gaia*: 377.3 ± 6.1 pc for HAT-P-37 and 667.7 ± 54.2 pc for the background star. Although we were able to recover the transit signal when the light curve is folded in orbital phase, it is impossible to measure reliable times of midpoint for the individual transits due to the contaminating light. 76 transit light curves were selected in the second stage of light-curve elimination, which resulted in a rejection of 15 light curves from open data bases. The linear + quadratic model is slightly better than the linear model in terms of ΔBIC and ΔAIC; this is not statistically significant (4.26 and 6.59, respectively). Therefore, we preferred the simpler linear model and corrected the ephemeris based on its parameters. The residuals from this model have a scatter less than 10 min. Since the number of data points is sufficient, and they are evenly distributed over a 10.033-yr baseline, we carried out a frequency search. We found that the peak with the maximum power (at a period of 61.87 d) has only 11.3 per cent FAP and so is not significant.

4 SUMMARY AND DISCUSSION

4.1 Discussion on the parameters of WASP-74 b

We attempted at a global model of WASP-74, which we found necessary before a TTV analysis of the system because the reference distance value in the literature ($d = 120 \pm 20$ pc; Hellier et al. 2015) of WASP-74 is smaller by more than 1σ from that measured by *Gaia* ($d = 148.029 \pm 1.037$ pc). Our results agree with that found by Mancini et al. (2019) in terms of both stellar and planetary parameters; hence, we confirm their findings, while masses and radii of both the host star and the planet are smaller compared to what had been found by Hellier et al. (2015). Our analysis was based on a confirmed value of zero eccentricity by the orbital phase of the occultation observation from Spitzer (Garhart et al. 2020), which ended the discussion on a potentially eccentric orbit. The evolutionary stage of the host star was found from MESA-isochrones (MIST) based on a global model of all available data and a semiempirically derived stellar radius. As a result, we found an age value of $3.43^{+1.00}_{-0.82}$ Gyr, consistent with and in between that given by Hellier et al. (2015) and Mancini et al. (2019).

4.2 Discussion on transit timing variations

We updated the ephemeris information of all 10 transiting exoplanets in our sample based on a homogeneously compiled set of mid-transit time measurements, resulting in the most precise light elements (T_0, $P_{\rm orb}$) so far, which will be useful for future observations. The ephemeris information listed in Table 4 is based on the most reliable light curves of each target owing to the selection criteria we employed and homogeneous measurements of the mid-transit times from models constructed with the same parameter sets. This approach also helped to decrease the scatter observed in the TTV diagrams for most of the cases significantly.

In each case, we compared the linear + quadratic model with the best linear model in terms of Bayesian and Akaike Information Criteria. On this basis, the linear + quadratic model was found superior only for WASP-14 b and WASP-69 b. However, there is a large gap of almost 4 yr in WASP-69 b's TTV data, which is composed only of 13 light curves. WASP-14 b has only 31 reliable light curves, which is also not sufficient to argue for a secular change in its TTVs. In such cases, addition of new precise data can change the situation dramatically as we experienced in the TTV analysis of

Table 8. Lower limits for the Reduced Tidal Quality Factors ($Q'_\star$) for the host stars in our sample in 95% confidence level. The lower limit for HAT-P-23 b has 99% confidence. The positive signs of the orbital period change in WASP-14 b and WASP-69 b are statistically significant. ΔAIC and ΔBIC values were used for comparisons between linear and quadratic models in this order. A negative value, therefore, means that the linear model should be favoured.

System	ΔAIC	ΔBIC	dP/dE (days/cycle)	$\dot{P}$ (ms/yr)	$Q'_\star$
HAT-P-23	−0.558	1.732	$(1.44 \pm 0.75) \times 10^{-10}$	3.7 ± 2.0	$>3.8 \times 10^{6*}$
WASP-37	−2.316	−1.831	$(-3.64 \pm 3.48) \times 10^{-9}$	-32.1 ± 30.7	$>5.0 \times 10^{2}$
WASP-69	17.987	18.472	$(9.96 \pm 2.32) \times 10^{-9}$	81.2 ± 19.0	–
WASP-74	7.813	9.368	$(-2.86 \pm 0.83) \times 10^{-9}$	-42.1 ± 12.4	$>5.0 \times 10^{3}$
HAT-P-56	−3.060	−2.288	$(0.13 \pm 1.09) \times 10^{-8}$	149.3 ± 124.0	$>1.2 \times 10^{3}$
WASP-2	−3.856	−2.005	$(0.09 \pm 2.43) \times 10^{-10}$	0.1 ± 3.5	$>5.7 \times 10^{3}$
WASP-14	20.422	21.856	$(4.84 \pm 0.83) \times 10^{-9}$	68.3 ± 11.7	–
HAT-P-32	−1.902	0.346	$(1.91 \pm 1.25) \times 10^{-10}$	2.8 ± 1.8	$>5.9 \times 10^{5}$
WASP-103	−4.062	−1.757	$(-3.23 \pm 6.64) \times 10^{-11}$	-1.1 ± 2.3	$>1.4 \times 10^{6}$
HAT-P-37	4.257	6.588	$(-2.41 \pm 0.77) \times 10^{-9}$	-27.2 ± 8.8	$>5.5 \times 10^{2}$

WASP-103 b. Before the inclusion of 10 precise light curves from Kirk et al. (2021), our results were in agreement with the finding of Maciejewski et al. (2018), Patra et al. (2020), and most recently Barros et al. (2022), which also lacks these data points of an increase in the orbital period against the expectation of an orbital decay from this ultra short-period hot Jupiter ($P_{\rm orb} \sim 0.926$ d). When the recent data were added, a negative quadratic coefficient was found. However, the quadratic model is not statistically superior to the linear model and the change in the orbital period is consistent with zero within less than 1σ.

We also searched for periodicity in the residuals from the linear model with Lomb–Scargle periodograms. However, we have not found any reliable periods in the transit timings of our targets smaller than a FAP value of 1 per cent other than that found in the TTV diagrams of WASP-69 b and HAT-P-56 b, which have only 13 and 16 points, respectively. We found a minimum FAP value of ∼5 per cent for WASP-14 b at 59.08 d, which also has the largest scatter in our sample with a range larger than 15 min. This planet has a non-zero eccentricity orbit ($e = 0.087 \pm 0.02$), confirmed by Spitzer occultation observations. Therefore, its TTV analysis should be refined in the future, with more data than the 31 reliable light curves that we selected and analysed.

We provide 35 new transit observations of the planets in our sample. They are shown in Appendix A and their data are included in the online materials. In addition, the mid-transit time measurements from our light curves and those of other observers, together with all the related statistics and information, are listed in a file for each of the planets in the online materials.

4.3 Discussion on tidal quality factors

We did not find any statistical evidence for either periodic or secular changes in the O–C diagrams of our targets, some of which are especially promising candidates (HAT-P-23 b and WASP-103 b in particular) to detect orbital decay. Since the tidal quality factor is an informative parameter for the efficiency of the host star ($Q'_\star$) to dissipate the energy arising from the tidal interactions with the close-in giant planet, we calculated lower limits for the reduced form of the parameter by making use of the formulae provided by Ogilvie (2014) and Maciejewski et al. (2018), the fifth percentile of the posterior probability distribution for the quadratic coefficient of the second-degree polynomial fits, and the system parameters we gathered from the references in Table 1 except for WASP-74 b for which we made use of our model values in Table 7 for consistency. We list these lower limits in 95 per cent confidence based on the results of our analyses of their respective O–C diagrams together with ΔAIC and ΔBIC values, showing why the quadratic models were not found to be statistically significant, and the rates of change in the orbital periods implied by the best-fitting quadratic functions in Table 8. The exceptions are HAT-P-23 (denoted with an asterisk in Table 7) for which we computed only the lower limit of $Q'_\star$ within 99 per cent confidence, and WASP-14 & WASP-69, for which the positive quadratic coefficient is statistically significant. Nevertheless, we cannot argue an increase in the orbital period for the planets in these latter two systems because we do not have enough data points sufficiently sampling the baseline.

HAT-P-23 and WASP-103 are two systems that deserve a mention for their tidal quality factors due to their very short orbital periods. Although a linear model was found to be superior to a quadratic model of the TTVs observed in HAT-P-23, we were able to constrain HAT-P-23's reduced tidal quality factor as $Q'_\star > 3.8 \times 10^6$ only in 99 per cent confidence. This value is in agreement with some of the theoretical expectations (Penev & Sasselov 2011; Penev et al. 2012; Ogilvie 2014; Hamer & Schlaufman 2019) while it exceeds some others (Jackson et al. 2008; Essick & Weinberg 2016). The value of the quadratic coefficient of the best-fitting parabola to the TTV diagram of WASP-103 b suggests an orbital period decrease with a rate of $\dot{P} = -1.1 \pm 2.3$ milliseconds per year. Although it is statistically inferior to the linear model and it is consistent with zero, given the magnitude of its uncertainty, a lower limit on the reduced tidal quality factor can be determined. Based on the stellar and planetary parameters from Gillon et al. (2014), we computed this limit as $Q'_\star > 1.4 \times 10^6$ for WASP-103 in 95 per cent confidence.

More observations, spanning longer baselines, are needed to reveal the nature of the TTVs expected from WASP-14 b (Mancini et al. 2019) based on its statistically significant non-zero eccentricity and any other target in our sample. The lower limit we derived for $Q'_\star$ is smaller than the 6.6×10^6 needed for it to survive on its orbit. There is an expectation for TTVs from WASP-2 b as well from the linear trend observed in the RVs of its host star. Baluev et al. (2019) found a positive derivative for the orbital period, which is supported by our finding ($\frac{\rm dP}{\rm dt} = (0.04 \pm 1.13) \times 10^{-10}$ s per year), although the quadratic fit was found to be inferior to a linear-only fit. All these systems need further and more precise follow-

up observations to reveal the nature of potential TTVs in them. Therefore, we urge observers to obtain more light curves with good photometric precision of these targets. Future observations from the TESS and CHEOPS satellites will help tremendously in terms of characterizations of these planets as well.

ACKNOWLEDGEMENTS

We gratefully acknowledge the support by the Scientific and Technological Research Council of Turkey (TÜBİTAK) with the project 118F042. We thank TÜBİTAK for the partial support in using T100 telescope with the project numbers 12CT100-378 and 16CT100-1096. We thank the observers in AUKR, UZAYMER, ATASAM, TUG, OBP, and IUGUAM observatories, and all the observers around the world who kindly shared their data with us. This research has made use of data obtained using the ATA50 telescope and CCD attached to it, operated by Atatürk University Astrophysics Research and Application Center (ATASAM). Funding for the ATA50 telescope and the attached CCD have been provided by Atatürk University (P.No. BAP-2010/40) and Erciyes University (P.No. FBA-11-3283) through Scientific Research Projects Coordination Units (BAP), respectively. Authors from Bilkent University thank the internship program of Ankara University Kreiken Observatory (AUKR). IST60 telescope and its equipment are supported by the Republic of Turkey Ministry of Development (2016K12137) and Istanbul University with the project numbers BAP-3685, FBG-2017-23943. We thank Jason Eastman for his help in using both versions of the EXOFAST code. New RV measurements from HARPS spectra are based on data obtained from the ESO Science Archive Facility under request number 556296. NA thanks Çukurova University Scientific Research Center with the project number FYL-2019-11726. NA also thanks TÜBİTAK National Observatory for its support in providing the CCD to UZAYMER. We thank all the observers who report their observations to ETD, ExoClock, and AXA open data bases.

DATA AVAILABILITY

Some of the light curves to derive mid-transit times were downloaded from Exoplanet Transit Database at http://var2.astro.cz/ETD/. All other light curves appearing for the first time in this article are presented as online material. Mid-transit times derived from our own light curves as well as that of other observers are presented as online data sets too. Individual radial velocity values derived from the HARPS instrument for WASP-74 b, which are being published for the first time within this study, are in the online data as well. We can also provide raw data sets of our own observations on request from the corresponding author.

REFERENCES

Adams E. R., Dupree A. K., Kulesa C., McCarthy D., 2013, AJ, 146, 9
Addison B. et al., 2019, PASP, 131, 115003
Agol E., Fabrycky D. C., 2018, in H.J. Deeg, Belmonte J.A., eds, Handbook of Exoplanets. ISBN:978-3-319-55332-0, Transit-Timing and Duration Variations for the Discovery and Characterization of Exoplanets, Springer, Cham, p. 797
Agol E. et al., 2021, Planet. Sci. J., 2, 1
Alam S. et al., 2015, ApJS, 219, 12
Anderson D. R. et al., 2014, MNRAS, 445, 1114
Astropy Collaboration 2013, A&A, 558, A33
Astropy Collaboration 2018, AJ, 156, 123
Bakos G. Á. et al., 2011, ApJ, 742, 116
Bakos G. Á. et al., 2012, AJ, 144, 19
Ballard S. et al., 2011, ApJ, 743, 200
Baluev R. V. et al., 2019, MNRAS, 490, 1294
Barros S. C. C. et al., 2022, A&A, 658, C1
Baştürk Ö., Hinse T. C., Özavcı Í., Yörükoğlu O., Selam S. O., 2015, in Rucinski S. M., Torres G., Zejda M., eds, ASP Conf. Ser. Vol. 496, Living Together: Planets, Host Stars and Binaries. Astron. Soc. Pac., San Francisco, p. 370
Baştürk et al., 2020, MNRAS, 496, 4174
Bergfors C. et al., 2013, MNRAS, 428, 182
Blanco-Cuaresma S., 2019, MNRAS, 486, 2075
Blanco-Cuaresma S., Soubiran C., Heiter U., Jofré P., 2014, Astrophysics Source Code Library, record ascl:1409.006
Blecic J. et al., 2013, ApJ, 779, 5
Bohn A. J., Southworth J., Ginski C., Kenworthy M. A., Maxted P. F. L., Evans D. F., 2020, A&A, 635, A73
Bouma L. G. et al., 2019, AJ, 157, 217
Bouma L. G., Winn J. N., Howard A. W., Howell S. B., Isaacson H., Knutson H., Matson R. A., 2020, ApJ, 893, L29
Cartier K. M. S. et al., 2017, AJ, 153, 34
Charbonneau D., Winn J. N., Everett M. E., Latham D. W., Holman M. J., Esquerdo G. A., O'Donovan F. T., 2007, ApJ, 658, 1322
Ciceri S. et al., 2015, A&A, 577, A54
Claret A., Bloemen S., 2011, A&A, 529, A75
Collier Cameron A. et al., 2007, MNRAS, 375, 951
Collins K. A., Kielkopf J. F., Stassun K. G., Hessman F. V., 2017, AJ, 153, 77
Skrutskie, M. F. et al., 2006, AJ, 131, 1163
Wright E. L., et al., 2010, AJ, 140, 1868
Daemgen S., Hormuth F., Brandner W., Bergfors C., Janson M., Hippler S., Henning T., 2009, A&A, 498, 567
Damiani C., Lanza A. F., 2015, A&A, 574, A39
Delrez L. et al., 2018, MNRAS, 474, 2334
Eastman J., Gaudi B. S., Agol E., 2013, PASP, 125, 83
Eastman J. D. et al., 2019, EXOFASTv2: A public, generalized, publication-quality exoplanet modeling code. preprint (arXiv:1907.09480)
Essick R., Weinberg N., 2016, ApJ, 816, 18
Evans D. F. et al., 2016, A&A, 589, A58
Ford E. B. et al., 2012, ApJ, 750, 113
Foreman-Mackey D., Hogg D. W., Lang D., Goodman J., 2013, PASP, 125, 306
Fulton B. J., Shporer A., Winn J. N., Holman M. J., Pál A., Gazak J. Z., 2011, AJ, 142, 84
Gaia Collaboration 2016, A&A, 595, A1
Gaia Collaboration 2018, A&A, 616, A1
Garhart E. et al., 2020, AJ, 159, 137
Gibson N. P., Aigrain S., Barstow J. K., Evans T. M., Fletcher L. N., Irwin P. G. J., 2013, MNRAS, 436, 2974
Gillon M. et al., 2014, A&A, 562, L3
Grimm S. L. et al., 2018, A&A, 613, A68
Hamer J. H., Schlaufman K. C., 2019, AJ, 158, 190
Hartman J. D. et al., 2011, ApJ, 742, 59
Hellier C. et al., 2015, AJ, 150, 18
Henden A. A., Levine S., Terrell D., Welch D. L., 2015, in American Astronomical Society Meeting Abstracts #225. Available at:https://ui.adsabs.harvard.edu/abs/2015AAS...22533616H/abstract
Høg E. et al., 2000, A&A, 355, L27
Honeycutt R. K., 1992, PASP, 104, 435
Huang C. X. et al., 2015, AJ, 150, 85
Ignatov V. K., Gorbachev M. A., Shlyapnikov A. A., 2020, Acta Astrophysica Taurica, 1, 13
Jackson B., Greenberg R., Barnes R., 2008, ApJ, 678, 1396
Joshi Y. C. et al., 2009, MNRAS, 392, 1532
Kirk J. et al., 2021, AJ, 162, 34
Knutson H. A. et al., 2014, ApJ, 785, 126
Lanza A. F., 2020, MNRAS, 497, 3911
Lendl M., Cubillos P. E., Hagelberg J., Müller A., Juvan I., Fossati L., 2017, A&A, 606, A18
Maciejewski G. et al., 2016, AcA, 66, 55

Maciejewski G. et al., 2018, AcA, 68, 371
Mallonn M. et al., 2019, A&A, 622, A81
Mancini L. et al., 2019, MNRAS, 485, 5168
Moutou C. et al., 2011, A&A, 533, A113
Ngo H. et al., 2015, ApJ, 800, 138
Nortmann L. et al., 2018, Science, 362, 1388
O'Rourke J. G. et al., 2014, ApJ, 781, 109
Ogilvie G. I., 2014, ARA&A, 52, 171
Patra K. C., Winn J. N., Holman M. J., Yu L., Deming D., Dai F., 2017, AJ, 154, 4
Patra K. C. et al., 2020, AJ, 159, 150
Penev K., Sasselov D., 2011, ApJ, 731, 67
Penev K., Jackson B., Spada F., Thom N., 2012, ApJ, 751, 96
Piskorz D., Knutson H. A., Ngo H., Muirhead P. S., Batygin K., Crepp J. R., Hinkley S., Morton T. D., 2015, ApJ, 814, 148
Poro A. et al., 2020, Astron. Lett., 47, 402
Raetz S. et al., 2015, MNRAS, 451, 4139
Rodrigo C., Solano E., 2013, in Guirado J. C., Lara L. M., Quilis V., Gorgas J., eds, Highlights of Spanish Astrophysics VII, Proceedings of the X Scientific Meeting of the Spanish Astronomical Society (SEA), held in Valencia, July 9 - 13, 2012. p. 953
Rodrigo C., Solano E., Bayo A., 2012, SVO Filter Profile Service Version 1.0, IVOA Working Draft 15 October 2012. Available at:https://www.ivoa.net/documents/Notes/SVOFPS/NOTE-SVOFPS-1.0.20121015.pdf
Sada P. V. et al., 2012, PASP, 124, 212
Schlegel D. J., Finkbeiner D. P., Davis M., 1998, ApJ, 500, 525
Seeliger M. et al., 2014, MNRAS, 441, 304
Simpson E. K. et al., 2011, AJ, 141, 8
Sousa S. G. et al., 2018, A&A, 620, A58
Southworth J., Evans D. F., 2016, MNRAS, 463, 37
Southworth J., Wheatley P. J., Sams G., 2007, MNRAS, 379, L11
Southworth J. et al., 2009, MNRAS, 396, 1023
Southworth J. et al., 2014, MNRAS, 444, 776
Southworth J. et al., 2015, MNRAS, 447, 711
Southworth J. et al., 2019, MNRAS, 490, 4230
Southworth J., Bohn A. J., Kenworthy M. A., Ginski C., Mancini L., 2020, A&A, 635, A74
Stassun K. G., Torres G., 2018, ApJ, 862, 61
Tregloan-Reed J. et al., 2018, MNRAS, 474, 5485
Triaud A. H. M. J. et al., 2010, A&A, 524, A25
Turner J. D. et al., 2017, MNRAS, 472, 3871
Vissapragada S. et al., 2020, AJ, 159, 278
Wallack N. L. et al., 2019, AJ, 158, 217
Wang Y.-H. et al., 2019, AJ, 157, 82
Wheatley P. J. et al., 2010, The thermal emission of the exoplanets WASP-1b and WASP-2b, preprint (arXiv:1004.0836)
White T. R. et al., 2018, MNRAS, 477, 4403
Winn J. N. et al., 2008, ApJ, 683, 1076
Wöllert M., Brandner W., 2015, A&A, 579, A129
Wöllert M., Brandner W., Bergfors C., Henning T., 2015, A&A, 575, A23
Zhao M. et al., 2014, ApJ, 796, 115
Zhou G., Latham D. W., Bieryla A., Beatty T. G., Buchhave L. A., Esquerdo G. A., Berlind P., Calkins M. L., 2016, MNRAS, 460, 3376
Zinn J. C., Pinsonneault M. H., Huber D., Stello D., Stassun K., Serenelli A., 2019, ApJ, 885, 166

SUPPORTING INFORMATION

Supplementary data are available at *MNRAS* online.

Please note: Oxford University Press is not responsible for the content or functionality of any supporting materials supplied by the authors. Any queries (other than missing material) should be directed to the corresponding author for the article.

APPENDIX A: LIGHT CURVES

We provide our own light curves (black data points) and EXOFAST-v1 models (red continuous curves) in Figs A1–A10.

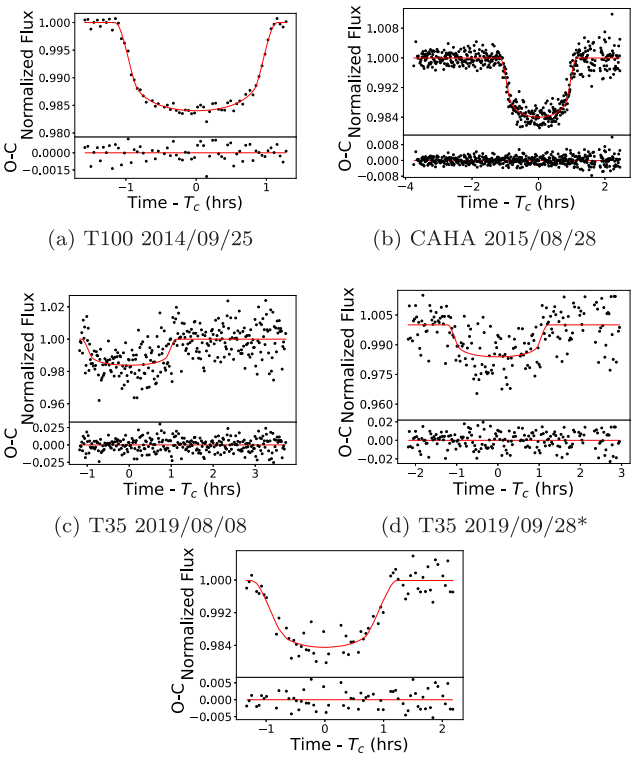

(a) T100 2014/09/25 (b) CAHA 2015/08/28 (c) T35 2019/08/08 (d) T35 2019/09/28* (e) UT50 2021/07/20*

Figure A1. HAT-P-23 b light curves. Black dots are data points while the red continuous curve is for the EXOFAST model in all the light curves presented in this section. The ones that were eliminated based on our quantitative light-curve selection criteria, therefore, not used in timing analyses are marked with asterisks.

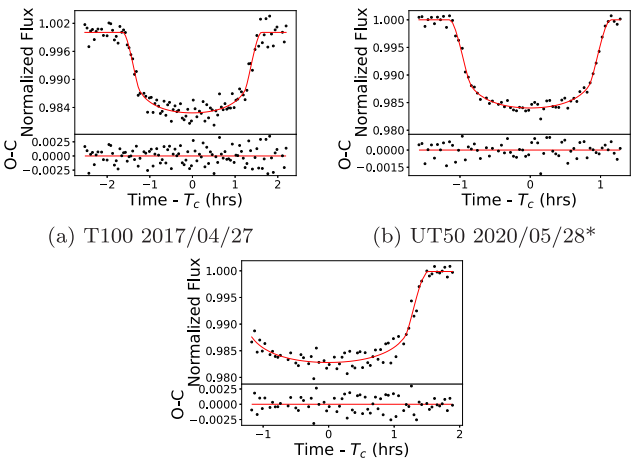

(a) T100 2017/04/27 (b) UT50 2020/05/28* (c) T100 2020/06/22*

Figure A2. WASP-37 b light curves.

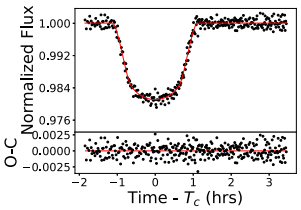

(a) CAHA 2015/08/22

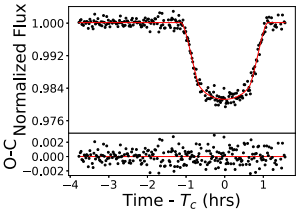

(b) CAHA 2015/09/18

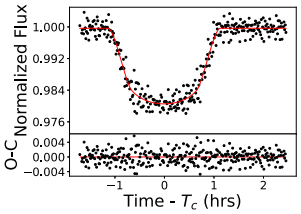

(c) CAHA 2016/09/08

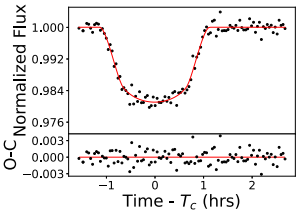

(d) T100 2016/10/09

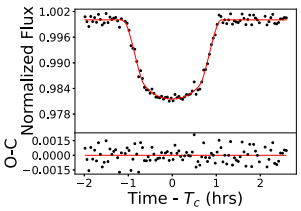

(e) T100 2017/08/26

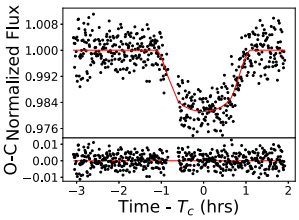

(f) T35 2019/07/27

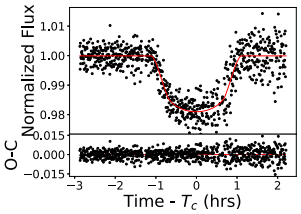

(g) T35 2019/08/27

Figure A3. WASP-69 b light curves.

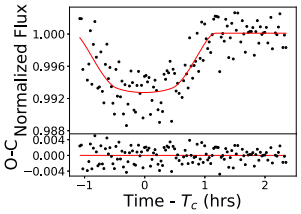

(a) T35 2019/07/07*

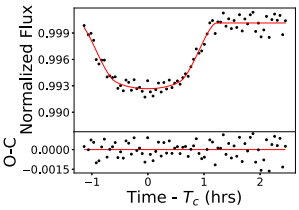

(b) T100 2020/08/12

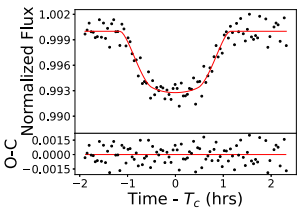

(c) IST60 2020/08/14*

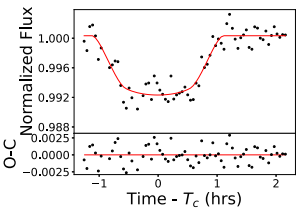

(d) T100 2020/08/27

Figure A4. WASP-74 b light curves.

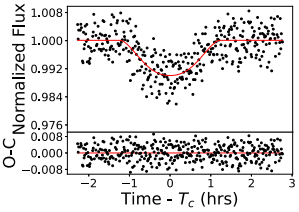

(a) T35 2019/02/17

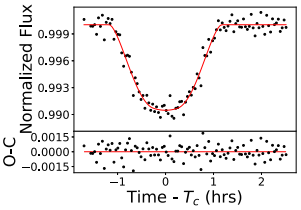

(b) T100 2019/11/09

Figure A5. HAT-P-56 b light curves.

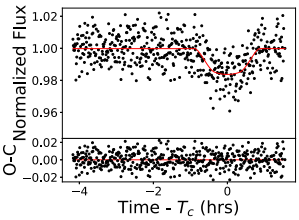

(a) T35 2019/07/20

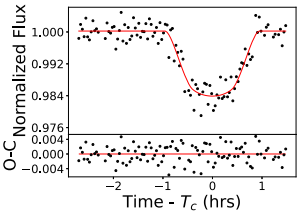

(b) ATA50 2020/10/12

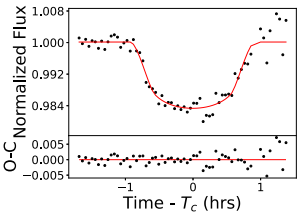

(c) T100 2020/10/25

Figure A6. WASP-2 b light curves.

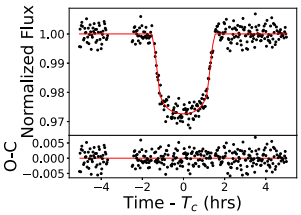

(a) T35 2019/11/03

Figure A7. HAT-P-32 b light curve.

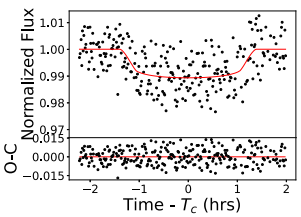

(a) T35 2019/07/03

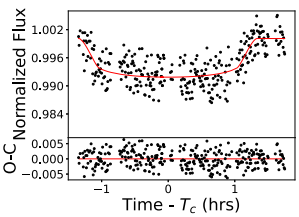

(b) ATA50 2020/05/14*

Figure A8. WASP-14 b light curves.

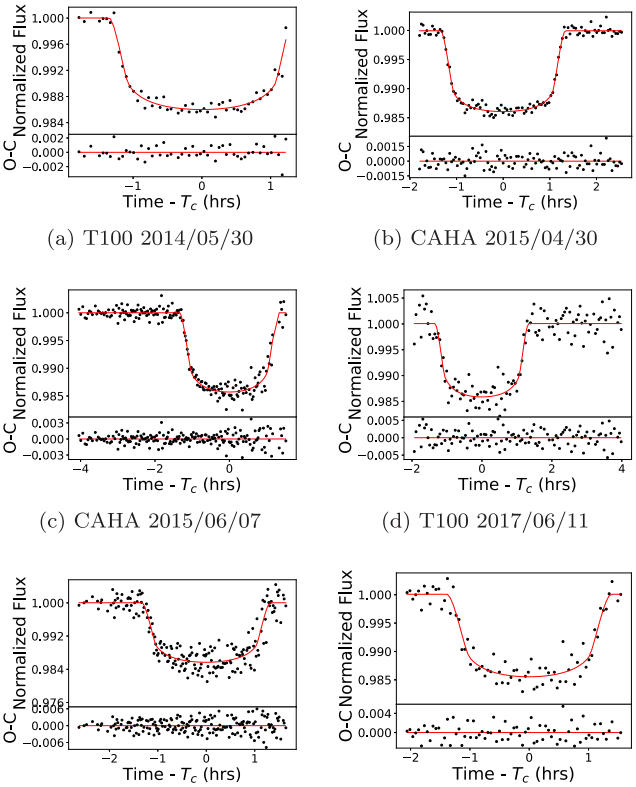

(a) T100 2014/05/30 (b) CAHA 2015/04/30

(c) CAHA 2015/06/07 (d) T100 2017/06/11

(e) T35 2018/07/01 (f) T100 2020/07/29

Figure A9. WASP-103 b light curves.

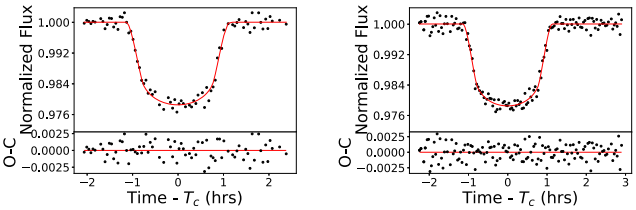

(a) T100 2015/08/04 (b) T100 2019/05/17

Figure A10. HAT-P-37 b light curves.

APPENDIX B: CORNER PLOTS

We provide the posterior probability distributions of the parameters of the linear fits to TTV data to illustrate the distributions as well as the correlations between the fit parameters.

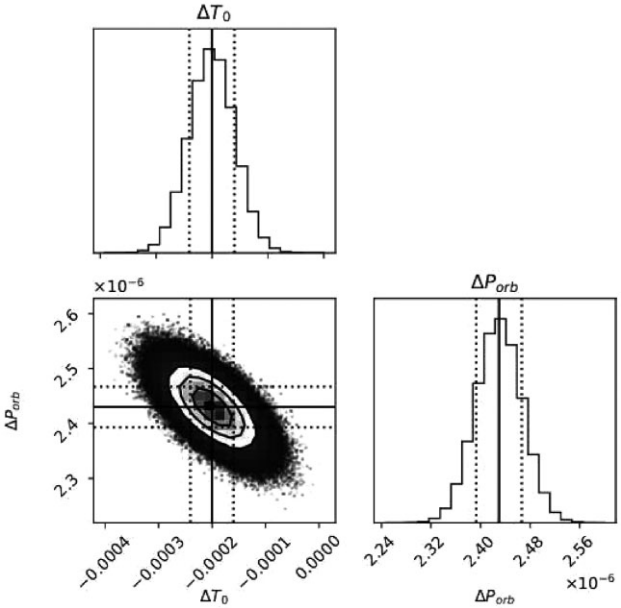

Figure B1. Corner plot showing the posterior probability distributions of the change in the reference mid-transit time (dT) (upper left) and the change in the orbital period (dP) (lower right), and the correlation between these two fit parameters (lower left) for HAT-P-23 b.

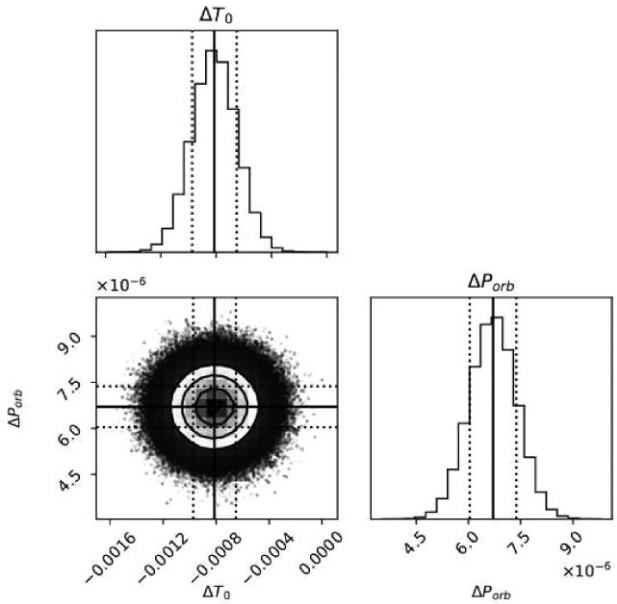

Figure B2. The same as Fig. B1 only for WASP-37 b.

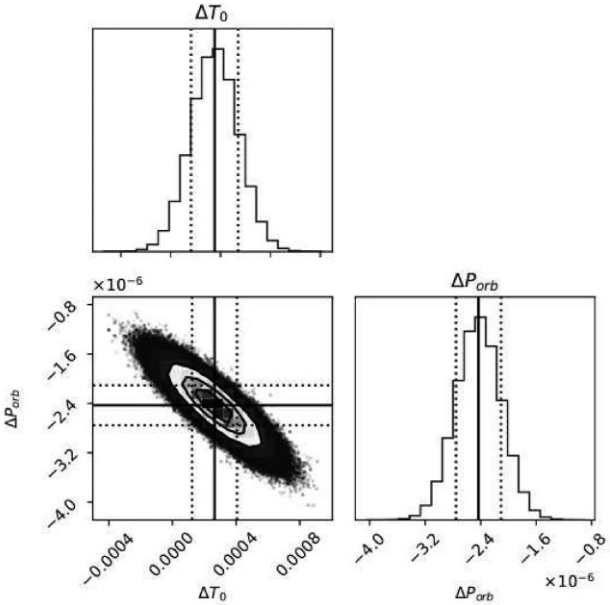

Figure B3. The same as Fig. B1 only for WASP-69 b.

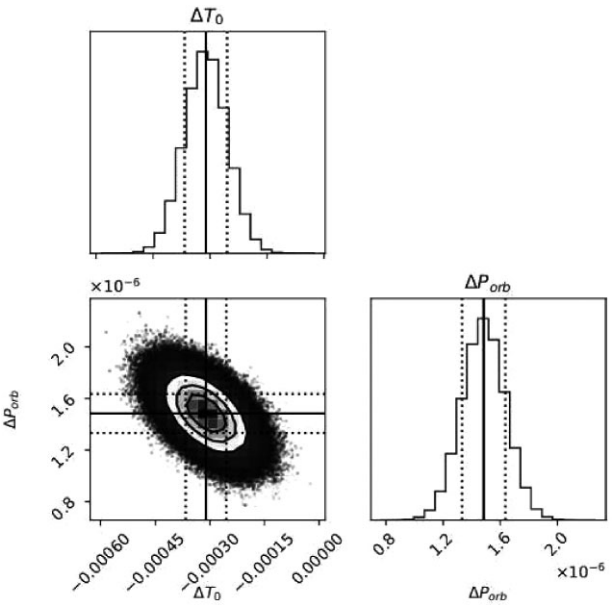

Figure B4. The same as Fig. B1 only for WASP-74 b.

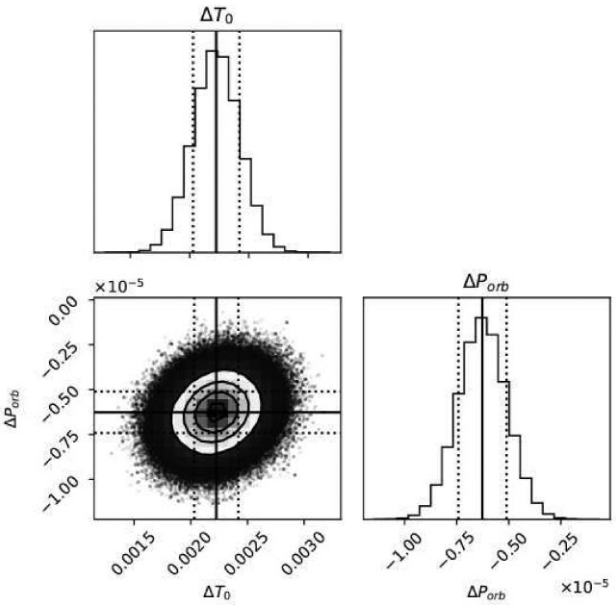

Figure B5. The same as Fig. B1 only for HAT-P-56 b.

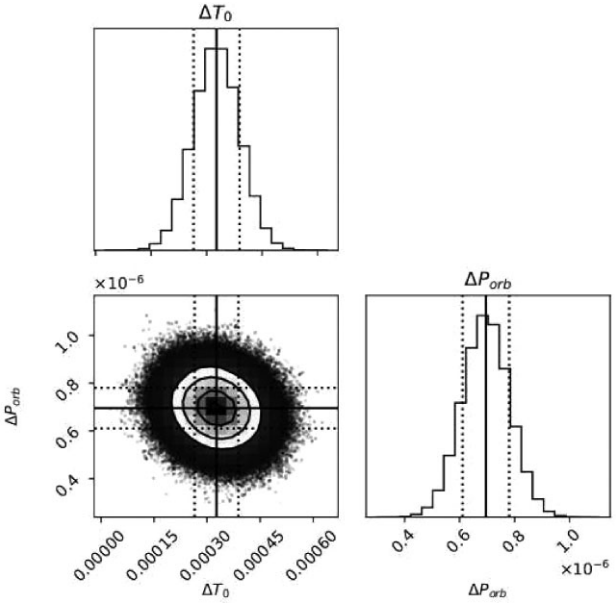

Figure B6. The same as Fig. B1 only for WASP-2 b.

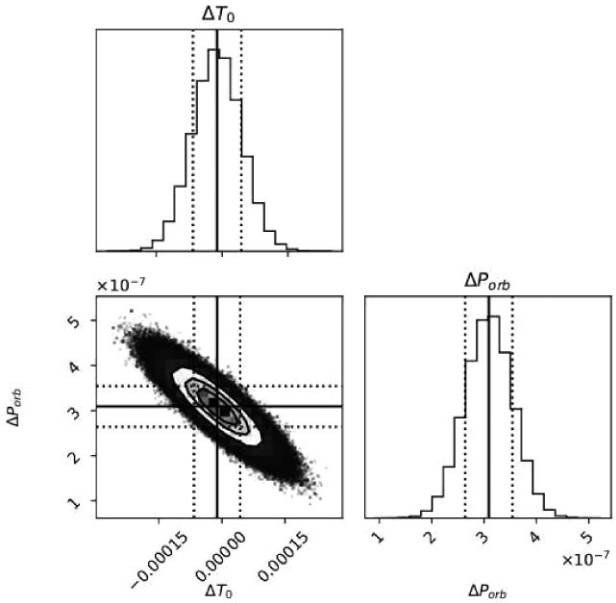

Figure B7. The same as Fig. B1 only for HAT-P-32 b.

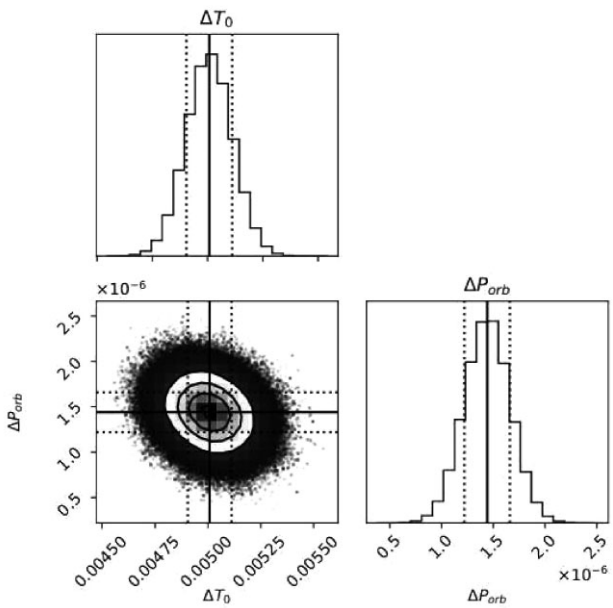

Figure B8. The same as Fig. B1 only for WASP-14 b.

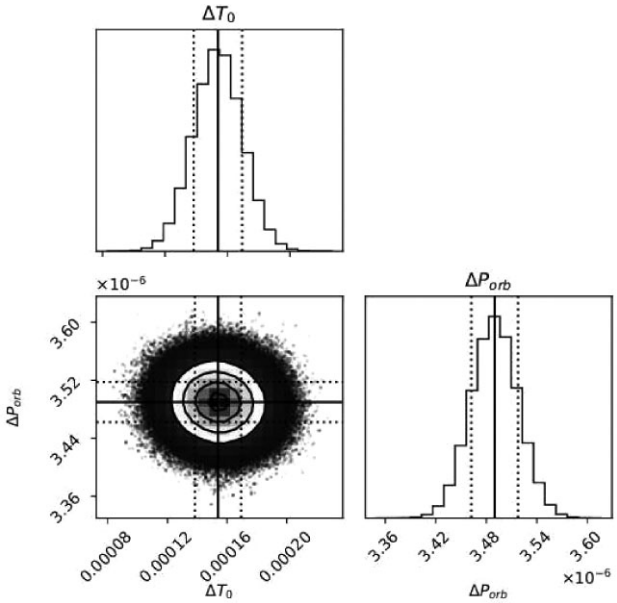

Figure B9. The same as Fig. B1 only for WASP-103 b.

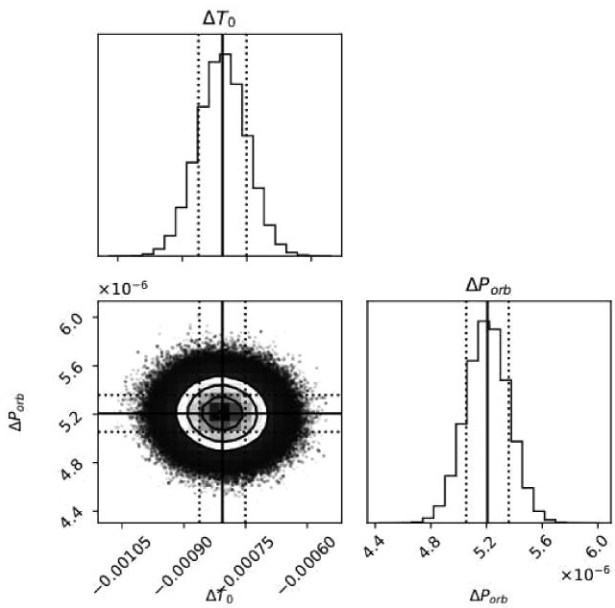

Figure B10. The same as Fig. B1 only for HAT-P-37.

This paper has been typeset from a TEX/LATEX file prepared by the author.